ABSTRACT

Title of Dissertation: BRILLOUIN CONFOCAL MICROSCOPY IN OFF-AXIS CONFIGURATION

Antonio Fiore, Doctor of Philosophy, 2021

Dissertation directed by: Professor Giuliano Scarcelli
Department of Bioengineering

Three-dimensional Brillouin confocal microscopy is an imaging modality that correlates with mechanical properties in biological media from subcellular to tissue level. Over the years we developed new approaches to this technique that improve the spectral performance and can measure directly the local refractive index as well as the complex modulus of the sample; to achieve this goal, we probed two co-localized Brillouin scattering geometries.

The confocal microscopy setting ensures three-dimensional mapping with high resolution, while the back scattering configuration allows access to the sample from the same side. For these reasons, such an instrument constitutes a new approach in investigating biological phenomena providing both local index of refraction and mechanical information with a single measurement. This technique has been improved in speed and spatial resolution in order to be applied to some specific challenging material characterization such as liquid-liquid phase separation.

BRILLOUIN CONFOCAL MICROSCOPY IN OFF-AXIS CONFIGURATION

by

Antonio Fiore

Thesis submitted to the Faculty of the Graduate School of the
University of Maryland, College Park in partial fulfillment
of the requirements for the degree of
Doctor of Philosophy
2021

Advisory Committee:

Professor Giuliano Scarcelli, chair
Professor Neil Blough
Professor Yu Chen
Professor Yang Tao
Professor Ian White

to the people that have been with me

Ackownledgements

This work has been made possible by the help, contribution, and effort of several people over the years. More than anyone, I would like to thank my advisor Giuliano. His endless commitment as a mentor traced the path for my scientific work and shaped my approach to scientific knowledge and academia. He is without a doubt the engine that drives everyone in our research group to achieve better and better results, day after day.

I would also like to thank my former lab mate Dr. Jitao Zhang for the great guidance and mentoring on optics and photonics. Thanks to Eitan, Christina, Josh, Romanus, Jake, Justin, Maggie, Eric and Chenchen for the endless days filled with discussions, debates, coffees, arguments, late night work, chess games and coding tips. I especially thank of Milos, Giulia and Romina for the great support inside and outside the lab, your friendship is worth more than a thousand citations.

A particular note of gratitude is due to Dr. Amal Isaiah and his team who collaborated and guided me on the intraocular pressure measurement project, and Carlo Bevilacqua who helped on aligning and characterizing the index of refraction measurement. Thanks to Jake for taking over and committing to the multi-geometry Brillouin microscopy project, and thanks to Eric for the great work on the coding and hardware control support.

Several people were crucial in my path even before arriving at University of Maryland. Kay introduced me to physics, Milena advised me during my

undergraduate research and thesis, Seemantini and Zeinab showed me new horizons in research beyond physics. I also would like to thank Carlo: co-author, friend, and fellow ambassador of knowledge.

Words can hardly express my gratitude towards my family, who supported me with all possible means. They motivate and encourage me every day to succeed in life. A world of gratitude goes to Madison; I would not be here without your love and your support, and most importantly your family welcomed me as an Allen from the first day.

Finally, I would like to thank my committee for taking the time to advise me and read this work. Along with them all faculty and staff of the Fischell Department, the University of Maryland graduate school, and the International Students & Scholar Services should also be praised for their incredible work and dedication. I am proud to be a Bioengineering Graduate Terp.

Table of Contents

List of figures

List of abbreviations

AFM:	Atomic Force Microscopy
BLS:	Brillouin Light Scattering
BSS:	Beam Steering System
CCD:	Charge-Coupled Device
CW:	Continuous Wave (Laser)
FC:	Fiber Coupler
FP:	Fabry-Perot
FWHM:	Full Width at Half Maximum
HWP:	Half-Wave Plate
LLB:	Lorentz-Lorenz Brillouin Coefficient
LLPS:	Liquid-liquid Phase Separation
MCD:	Maximum Common Divisor
NA:	Numerical Aperture
PBS:	Polarizing Beam Splitter
PSF:	Point Spread Function
QWP:	Quarter Wave Plate
RI:	Refractive Index
SBR:	Signal-to-Background Ratio
SBS:	Stimulated Brillouin Scattering
SMF:	Single Mode Fiber
SNR:	Signal-to-Noise Ratio
VIPA:	Virtually Imaged Phased Array
3PFP:	Triple Pass Fabry-Perot

CHAPTER 1: INTRODUCTION

1.1 The physics of Brillouin Light Scattering

1.1.1 Origin of Brillouin scattering

In this introductory chapter we will introduce the physics of Brillouin Light Scattering. Brillouin light scattering (BLS) is usually defined as the inelastic scattering of light in a physical medium by periodic modulations of the dielectric constant in a medium [1-3]. Such phenomenon can be driven by spontaneous fluctuations within the medium i.e., spontaneous Brillouin scattering, or stimulated through a non-linear optical coupling i.e., stimulated Brillouin scattering (SBS) [4].

The dielectric constant modulation can have different origins: the most commons are vibrational oscillations (phonons) and magnetic oscillations (magnons) [5]. Vibrational oscillations, which are the one this thesis will focus on, can have different origin and modes. Acoustic phonons are usually described as collective pressure waves within materials, that travel in adiabatic conditions. Optical phonons are instead vibrational modes of atoms within their equilibrium position, and their description explains Brillouin zones in crystals and Raman scattering events [6]. This blurred line between the description of Raman and Brillouin scattering is due to the history: the two phenomena have been discovered and studied in the same years [1,7], and experimentally investigated at the same time. The one fundamental difference between the two is that Brillouin is based on a collective motion along a defined direction, while Raman scattering excites vibrational mode of molecules; from an experimental standpoint this translates in a strong angle dependence of Brillouin scattering, while Raman scattering remains substantially isotropic [8].

One last consideration that needs to be addressed in on the origins of acoustic phonons. In absence of external perturbation and in thermodynamic equilibrium, the baseline distribution of phonon is completely dependent of statistical thermodynamics based of Boltzmann distribution [2,8]. In these conditions, the population of acoustic phonon in a material is temperature dependent and a direct result of thermal motion of atoms and molecules. Hence the name of thermal acoustic phonons. In this dissertation, unless otherwise noted, we will refer with the words 'Brillouin scattering' to spontaneous Brillouin light scattering from thermal acoustic phonons.

Prediction of the BLS became possible with the development of the theory of thermal fluctuations in condensed matter at the beginning of the 20th century. With the studies of Smoluchovskii, Einstein and Debye [9-11], the thermal fluctuations of density can be considered as a superposition of the acoustic waves (thermal phonons), propagating in all directions in condensed media. Later, the work of Landau and Plazcek [12,13] clarified the thermodynamic nature of thermal phonons and gave a complete picture of the Rayleigh-Brillouin scattering spectrum.

1.1.2 Fundamental equations of Brillouin Scattering

Let's then consider a thermal acoustic phonon traveling through a material. For the sake of simplicity in this first instance we will assume no acoustic attenuation, and a transparent homogeneous media. Such acoustic wave will be described by a frequency Ω, a wavevector $\mathbf{q}$, and a dispersion relationship $\Omega = qv$ where v is the propagating speed of the sound wave. Similarly, we can consider an incident photon traveling in the same material, described by a frequency ω_i, wavevector $\mathbf{k_i}$, and dispersion relationship $\omega_i = k_i c/n$. At the scattering event, a scattered photon is emitted, with frequency ω_s and wavevector $\mathbf{k_s}$. Being the wavevector

arbitrary, they are not assumed to be parallel. Thus, we define θ as the angle between $\mathbf{k_i}$ and $\mathbf{k_s}$.

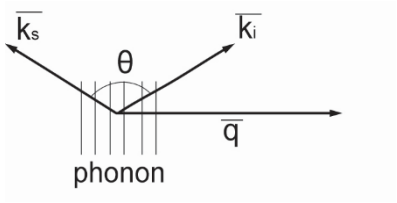

Figure 1.1 Schematic of photon-phonon scattering

The interaction between these two waves can be described with phase matching conditions on frequency and wavevector that define conservation of energy and momentum in the scattering event:

$$\omega_s = \omega_i \pm \Omega \tag{1.1}$$

$$\mathbf{k_s} = \mathbf{k_i} \pm \mathbf{q} \tag{1.2}$$

The $\pm$ sign express the possibility of a phonon traveling in both directions of propagation, which gives rises to a sort of Doppler effect. On a semiclassical quantum mechanics standpoint, phonons can be described as quantization of the thermal energy [2,8]. This description, like the quantization of light that introduced the photon, allows an intuitive description of the Brillouin scattering event: this splitting is described as the creation or annihilation of a phonon following the scattering event as result of the gain or loss of energy of the scattered photon [6]. Since the typical frequency of the phonon (~GHz for thermal acoustic phonons) is extremely low compared to the frequency of the photon (~10 THz in the visible range) [11,13], we can approximate $k_i \cong k_s$. Thus $q = 2k_i \sin\theta/2$. Using the dispersion relationship for photon and phonon, we obtain an expression for the Brillouin frequency shift:

$$\Omega = \frac{2\omega_i n v}{c} \sin\frac{\theta}{2} \qquad 1.3$$

the shifted frequencies will appear in the spectrum of the scattered light alongside the central elastically scattered light component [14], as shown in the figure below:

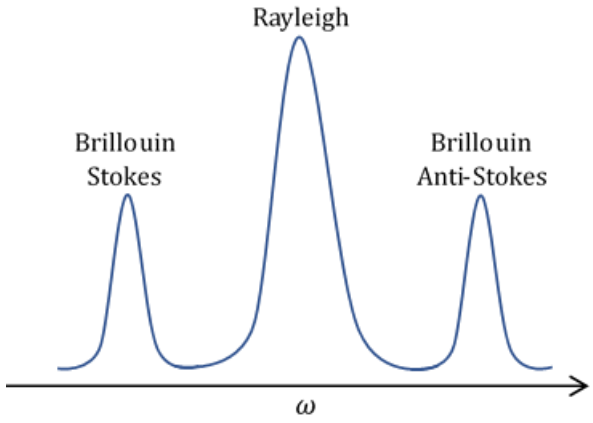

Figure 1.2 Spectrum of scattered light including Rayleigh peak (elastic) and Brillouin double-peak (inelastic). The Stokes components are the ones with an energy lower than the incident photon, while anti-Stokes components have higher energy photons.

The fundamental aspect of the phenomenon that many scientists immediately recognized as particularly valuable in investigations of condensed matter is the link between the light frequency and the material properties, through the speed of the phonon v (eq. 1.3). This quantity depends on a variety of factors both thermodynamical and mechanical. In particular, the speed of sound can be defined as the square root the stiffness tensor divided by the density [11,13]:

$$v = \sqrt{c_{ij}/\rho} \qquad 1.4$$

The stiffness tensor components c_{ij} relate the stress and strain induced by the phonon at the frequency Ω, while the density ρ is a quantity that can be related to the thermodynamic

state of the atoms or molecules that vibrate as the phonon propagate. It comes to no surprise then, that Brillouin scattering experiments were conducted to investigate liquids, solids, gas and crystals mechanics and thermodynamics since its discovery [15,16]. After a considerable amount of time Brillouin spectroscopy also found its application also in the biological realm [17-20].

1.2 Traditional Brillouin light spectroscopy

In this section we will discuss advancements made in the state of the art of Brillouin spectroscopy, from classical instruments to more recent technologies. Optical spectroscopy is based on the spatial separation of light into its spectral components achieved by light dispersive elements in conjunction with a photon detector. A critical quality metric for spectral analysis and processing is the dynamic range, defined as the ability of the spectrometer to simultaneously measure signals, i.e. different frequencies, characterized by large difference in intensities. The dynamic range of a spectrometer is determined by the dynamic range of the photon detector and by the spectral contrast (also sometimes referred to as spectral extinction) of the dispersive process, i.e. the fraction of a spectral component incorrectly detected in neighboring spectral channels.

Brillouin spectroscopy refers to any spectroscopy technique aimed to the quantification of Brillouin frequency shift, and more in general, to the acquisition of Brillouin spectra. As mentioned in paragraph 1.1.2, Brillouin frequency shift in visible light is a variation of about ~0.1%, which corresponds to a frequency shifts range of 1-10GHz. Using Rayleigh criteria for peak resolution, we can define a bottom limit for the resolution of an instrument built for this

purpose: 0.5-5GHz (or 0.005-0.05 nm), which corresponds to ½ of the measured frequency shift.

The spectral contrast requirements can also be estimated based on simple considerations and empirical data: Brillouin scattering cross section is typically in the order of 10^{-9}. Assuming a homogeneous transparent, the elastically scattered light in the backscattering direction is ~0.1%. This means that the spectral extinction of the spectrometer combined need to be at least $1/10^{-6}$, which corresponds to 60dB. If the medium is not transparent additional extinction is also required to compensate for refractive index inhomogeneities and multiple scattering events. In conclusion, based on observation made over several decades, transparent and quasi-transparent biological media such as corneal tissue and single cells require spectral extinction in the order of 60-70dB in backscattering configuration [21,22], while more scattering material such as connective tissue, cartilage and atherosclerotic plaques can require from 85dB up to 100dB [23,25].

1.2.1 From echelle grating to Fabry-Perot interferometers

The first experimental reports detection of such phenomenon only appeared in the scientific literature in the August of 1930 thanks to Evgeni Gross [15]. This gap reflects both the process of understanding the particle nature of light together with the newborn field of quantum mechanics, as well as a technical limitation due to lack of high-resolution spectrometers. In 1930 Gross reported the use of Echelon (or echelle) grating in a 30-step configuration. Such instrument was only introduced in 1898 by A. Michelson [26], just over thirty years before Gross' experiment. An approach based on diffraction grating remain the most popular, despite clear limitations in spectral resolution and contrast that limited experiments to transparent homogeneous materials like liquids or crystals [27]. It will take two

major technological advancements for a new class of Brillouin spectroscopy instruments to be born: a cavity-based light analyzer, the Fabry-Perot interferometer, and a cavity-based light source, the laser.

Fabry and Perot described their interferometer in 1899 [28], almost coincidentally with Michelson's echelon grating. However, in order for such interferometer to be used in spectroscopic measurement, a frequency scanning mechanism was needed, and indeed it arrived between 1949 [29], being then implemented first to light spectroscopy in general in 1955 [30,31], and to Brillouin spectroscopy specifically in combination with a laser in 1964 [32]. A Fabry-Perot cavity is formed by two partially reflective surfaces parallel to each other (Figure 1.3a); these surfaces form a cavity in which light is transmitted with an efficiency proportional to the reflectivity of the surfaces of the cavity. If the frequency is resonant in the cavity, meaning the condition $\lambda = 2d$ is satisfied, where d is the distance between the surfaces. In that case the light is reflected multiple times in the cavity and its transmission is optimized. The range of frequency available is defined as the Free Spectral Range (FSR), and it can be though as the distance in the frequency space between two consecutive interference orders. The resolution in the spectral space $\delta\nu$ is defined as the minimum difference between two frequencies that are correctly resolved. Thus, we can now define the finesse coefficient $F = FSR/\delta\nu$. An intuitive interpretation of the finesse is a quantification of the number of bounces that light undergoes within the cavity, and it depends on the reflectivity of the surfaces as:

$$F = 4R/(1 - R^2) \tag{1.5}$$

The transmission of the resonant frequency will be

$$T = \frac{1}{1 + F^2 \sin^2(\phi/2)} \tag{1.6}$$

Where ϕ is the induced phase retardance in the transmitted beam. This also sets the maximum contrast achievable as ~F^2, calculated as the ratio between the maximum and the minimum of the transmission function T. While the resonant frequency is transmitted, non-resonant frequencies are not dispersed but rather reflected, with a loss function that equals 1-T, for energy conservation.

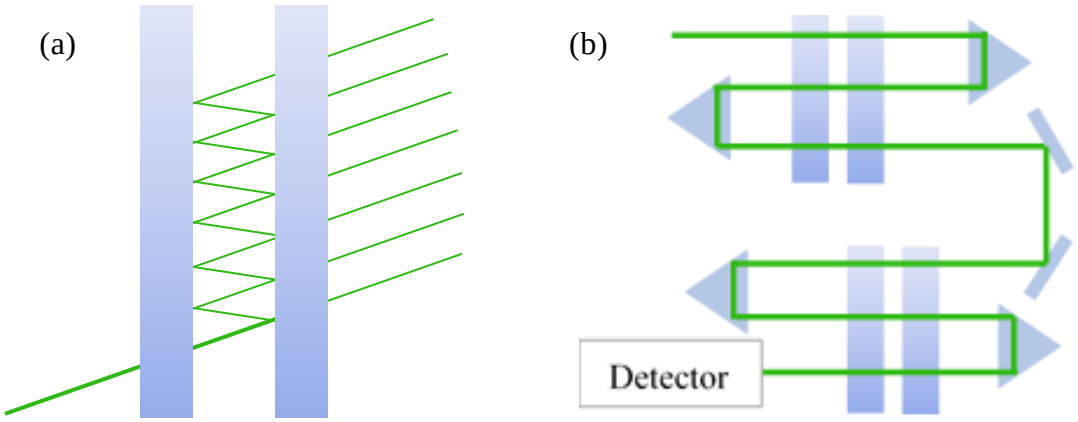

Figure 1.3 Principles of Fabry-Perot spectroscopy. (a) Schematic of Fabry-Perot cavity resonance. (b) Schematic of Sandercock's six-pass tandem Fabry-Perot interferometer. Each time the beam passes through a cavity, the spectral contrast is further increased based on the resonant frequency of the cavity.

The advantage of Fabry-Perot interferometer is the ability to reach remarkably high finesse values [33], which is crucial to reach sufficient spectral resolution to separate elastic scattering from Brillouin components. However, as showed in Eq. 1.6, the higher the finesse, the lower the optical throughput.

In 1970 John Sandercock pushed even further the use of Fabry-Perot cavities introducing a multipass tandem interferometer [34]. This instrument, which became a standard in Brillouin spectroscopy for many years, relies on two air-spaced Fabry-Perot cavities [35].

The scattered light passes through each cavity three times for a total of six passes. The resonant frequency of the cavities is adjusted by changing the distance between the reflective surfaces in the cavity. The tandem effect refers to the alignment of the two cavities to pass the same frequency, and thus combining the spectral contrast of all the etalon passes. As a comparison, if we wanted to build a system with similar contrast based on a single etalon with such contrast would require surface reflectivity greater than 99.999%, which is more than most industry standards, and would have an extremely poor throughput. For this reason, this instrument continues to be used today in many Brillouin spectroscopy applications that require contrast above 100dB [36].

An alternative to scanning Fabry-Perot interferometry is a tilted Fabry-Perot etalon configuration; particularly, when the light is focused with a non-zero incident angle in a Fabry-Perot cavity, such angle creates multiple potential resonant paths, so that multiple frequency can be transmitted at the same time. The different frequencies will only resonate at a given angle of propagation, and therefore will exit the cavity with such angle. Frequency that are greater than the FSR will superimpose on the same position, creating an ambiguity of $\pm nFSR$, where n is an integer. Thus, spectroscopy with such approach is possible only as long as the incident central frequency as well as the range of Brillouin shift values are known. In this way it is possible to obtain the full spectrum within the FSR boundaries, in a single camera acquisition [37]. However, this multiplexing does not significatively increases the acquisition speed because the throughput function does not fundamentally change, thus leaving unchanged the loss profile as well. However, we do note the advantage of eliminating the requirement for any scanning mechanism [38,39].

1.2.2 Brillouin Spectroscopy through Virtually Imaged Phased Arrays

As we have seen in the last paragraph, a tilted Fabry-Perot will transmit all frequencies with an angular dispersion, in a range of $\lambda_0 \pm$ FSR, allowing single shot spectra acquisition. Similarly to a tilted Fabry-Perot etalon, a VIPA (Virtually imaged phased array) is an etalon in which the light self-interferes because of multiple reflections within the etalon itself. However, unlike the tilted Fabry-Perot, in a VIPA the back surface comes with a 100% reflective coating, which dramatically reduces insertion losses and increases the throughput up to 80%. Like in Fabry-Perot based approaches, also VIPA etalons have been cascaded in two-stages and even three-stages configurations [41], although cascading VIPA etalons requires dispersion along different axis to guarantee the spectral contrast enhancement [40]. Hence, the configuration with two VIPA etalon stages in a cross-axis configuration became a standard because of its compromise between spectral contrast, optical throughput, and finesse [42].

1.2.3 Two stage cross-axis VIPA spectroscopy

The most used spectrometer for fast acquisition of the Brillouin spectrum is the VIPA spectrometer, as reported in Figure 1.4. The scattered light collected from the microscope is collimated at the exit of the optical fiber, resulting in a round Gaussian beam. The cylindrical lens C1 focuses the light in a line at the entrance of the VIPA 1. Then, the VIPA pattern is collimated with a second cylindrical lens C2, and filtered with a horizontal mask. Similarly, in the second stage the light is focused in a line again using a spherical lens SP1, it enters the VIPA 2 and it is collimated and filtered with a second spherical lens SP2 and a vertical mask. The VIPA pattern obtained in finally imaged on a CCD sensor using an achromatic pair. The final pattern is given by the intersection of the single VIPA patterns overlapped, resulting in a dots pattern in which the overall FSR is on the diagonal direction.

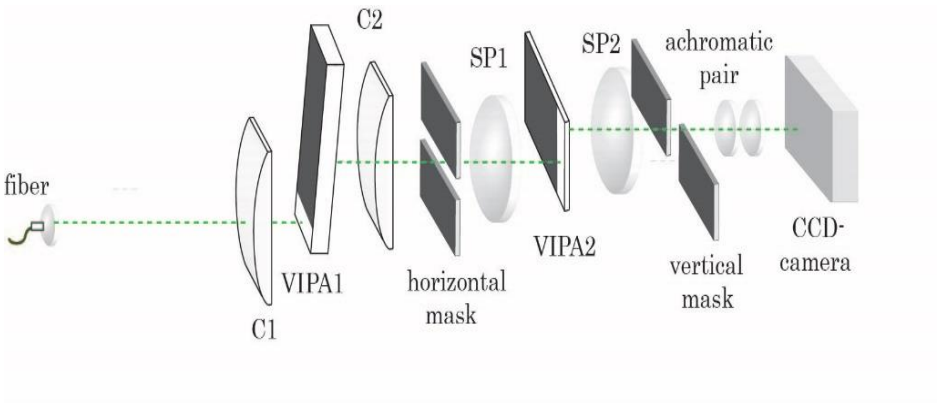

Figure 1.4 Schematic of two stage cross-axis VIPA spectrometer.

The spectral extinction ratio, or simply extinction ratio, is probably the most important parameter of a Brillouin microscope, because it expresses how well the elastic scattering light is suppressed. To measure the extinction ratio, it is necessary to acquire multiple spectral acquisition of the laser light (i.e. when there is no sample loaded) with different signal conditions. The signal is generally adjusted by varying the laser power, the exposure time, or the gain of the camera.

However, this is not the only parameter that counts. In fact, with a VIPA etalon it is possible to reach about 65% light efficiency in effective throughput, which means that a two stage VIPA has an optical throughput of about 35-40% [42]. The amount of light that reaches the CCD camera determines the maximum acquisition speed. This further explains why a two stage VIPA spectrometer is the preferred solution.

1.3 Biophysical background of Brillouin microscopy

The scientific publications of Brillouin light scattering for biological applications begins in 1979 with the measurement of collagen samples by Cusack and Miller [18]. Right after, Vaughan and Randall also proved the possibility of measuring biological media,

specifically corneal tissue and crystalline lens [17]. These experiments highlighted the potential of biomechanical investigation through Brillouin light spectroscopy, with the goal of measuring mechanical modifications using this label-free light-based approach.

Nevertheless, we had to wait until 2008 for an imaging implementation of BLS that was able to map in three dimensions in biological media. The fundamental advancement in this direction is the introduction of VIPA-based spectroscopy [22] in combination with a confocal microscope, thus the subsequent birth of Brillouin confocal microscopy [43]. Since then, several studies have been conducted on both cellular level and tissue level exploring the mechanical cues at cellular and tissue level [44-46]. Despite the importance of these improvements, the contrast of VIPA-based spectrometers remained not comparable to scanning multipass Fabry-Perot devices. Thus, the ability to improve the spectral contrast of our fastest instrument, i.e. the VIPA spectrometer, can be the key to access samples that are now outside the range of measurement of both solutions.

Despite the complexity of describing phonon propagation in biological media [47], strong correlations between the frequency shift observed in the samples and the mechanical properties has been verified in several instances with comparative measures between Brillouin microscopy and AFM, shear rheometer, compressive stress test, and more [43,48,49]. Moreover, experiments with specific biomarkers that induce known effects in cells and tissues produced results in accordance with this hypothesis [43,44,49-51]. In other words, even though biological media presents a step up in complexity compared to crystals, pure liquids or ideal gases, Brillouin frequency shift can be a proxy for biomechanical cues. This first order approximation remains valid considering water-based materials in which a strong correlation between refractive index and density can be identified. Looking at equation 1.3 and 1.4, it self-

evident how such conditions lead to a direct correlation between Brillouin frequency shift and stiffness.

1.4 Scientific advancements and contributions

The considerations of this first chapter will be generalized and expanded later in the thesis. However, few fundamental points can be summarized to outline the current state of the art of Brillouin confocal microscopy, and with it we can outline the main goals of this dissertation:

1. The frequency shift induced by BLS is extremely small compared to the frequency of the incident light. This, combined with the strength of the unshifted Rayleigh scattering peak and back reflections in biological media, sets the bar for the performance of Brillouin spectrometers built for bioimaging purposes: extremely high resolution and excellent spectral contrast. The current state of art of Brillouin microscopy is perfectly able to image biological media that are transparent or translucent. However, in recent years the need for higher contrast increased with the growing interest towards more complex, inhomogeneous, and optically opaque biological samples. This growing interest is also testified but the rising number of attempts to break the contrast limit of Brillouin spectrometers, accessing biomechanical measurement in amyloid plaques, atherosclerotic plaques, bone tissue, and more [23-25,33,45]. These diversified efforts of the Brillouin bioimaging community testify an incomplete research that aims to find a suitable solution for fast yet efficient Brillouin spectroscopy in highly scattering media. Thus, in chapter 2, we will explore some technical advancements in this

direction, showing potential solution to increase both spectral extinction and spectral resolution of VIPA spectrometers.

2. Brillouin frequency shift is strongly dependent on the scattering angle. Such dependance has been and can be exploited to retrieve material properties beyond the simple frequency of the phonon. Material scientists and physicists are aware of such correlation, which led Brillouin spectroscopy to become a tool to measure several thermodynamic and optical properties, including refractive index. To best of our knowledge such approach has never been implemented in a microscopy setup with clear intent measure refractive index. Such an achievement would open a new front in refractive index mapping which traditionally relies on quantitative phase imaging, and thus limited to simple objects (like single cells) with two side access requirements. In Chapter 3 the angle dependency will be used to derive a way to directly measure the refractive index and the speed of sound in a three-dimensional sample. We implemented such technique in a confocal microscope, showing direct refractive index mapping, in three dimensions using two photon-phonon scattering geometries, with single side access to the sample. Thanks to this novel approach to Brillouin microscopy, we enabled refractive index mapping of samples that is not achievable with traditional techniques, such as in vivo cornea, or complex cell aggregates.

3. The measurement of the frequency shift is correlated to hydromechanical properties in water-based biological material, because of a strong correlation between density and refractive index is such materials. However, this correlation is not universal because of the complexity of the phonon-photon scattering, which depends on viscoelasticity, refractive index, and density of the sample at the same time. This weak

spot in the Brillouin biomechanical characterization has been highlighted by several attempt to measure samples that are not water-base, like adipocytes or lipid aggregates [45,46], showing strong artifacts. Even the knowledge of refractive index will not solve such artifact since the speed of sound is still dependent on both modulus and density. Therefore, only a measurement that successfully probes refractive index, density together with Brillouin frequency shift can aim to correctly retrieve the mechanical cues outside the water-based realm of materials. In Chapter 4, we will describe a novel approach to Brillouin microscopy that aims to exploits measurements of frequency shift, linewidth and intensity at different angles to retrieve refractive index, viscoelasticity and density from the same confocal volume, leading to a complete optical and mechanical characterization of the sample.

CHAPTER 2: ADVANCEMENTS IN BRILLOUIN LIGHT SPECTROSCOPY

In this chapter we report different implementations of Brillouin VIPA spectrometers with different specific aim in each case. First, we will describe the use of a Fabry-Perot etalon as an add-on filter modification to improve the contrast of existing cross axis VIPA spectrometers; such upgrade made possible Brillouin spectroscopy measurement in highly scattering samples like intralipid solutions and animal muscle tissue. Then, we will prove the possibility of building an extremely compact two-stage VIPA spectrometer with a single etalon in which light is recirculated. We experimentally demonstrate that such approach can have substantially the same performance as traditional instruments. Finally, we introduce the concept of single-axis VIPA spectroscopy. Dispersing light along a single direction we enabled the cascading of multiple VIPA elements without loss in spectral resolution. We built the first instrument of this kind with three-stage VIPA dispersion, showing superior performance when compared to cross-axis instruments.

2.1 High-extinction VIPA-based Brillouin spectroscopy

Here we report a spectrometer configuration featuring a tunable, high-throughput and narrow-bandpass filter based on a low-finesse Fabry Perot etalon[1]. Thanks to this innovation, we increased the overall spectral extinction by more than ten-fold with respect to state-of-the-art spectrometers with less than 2 dB insertion loss. This enabled us to perform rapid Brillouin

[1] This section is based on a published peer-reviewed article [52]

spectral characterization deep into nontransparent biological tissue without any limitation due to elastic scattering background.

The spectrometer consists of a triple-pass Fabry-Perot (3PFP) bandpass filter and a two-stage VIPA spectrometer (Fig. 2.1). The 3PFP filter was placed on the collimated beam path, before a two-stage VIPA spectrometer featuring two VIPA etalons of 17 GHz Free Spectral Range (FSR). To build the 3PFP, we used a fused silica etalon of 3.37 mm thickness (i.e., 30 GHz FSR) coated for 60% reflectivity, resulting in low finesse [53]. Using low reflectivity and low finesse, the etalon in single-pass configuration has a 5 GHz bandwidth with <10% loss. However, at low finesse, the spectral extinction is limited to 11 dB. Using a triple-pass configuration, the filter featured a 3 GHz bandwidth and 40% insertion loss. The throughput of the filter is less than the ideal case (<15%) because of secondary resonant cavities formed between the mirrors and the etalon due to the multi-pass configuration. Nevertheless, for equal rejection performances, the multi-pass low-finesse approach is twice as efficient as a high-finesse single pass configuration [54].

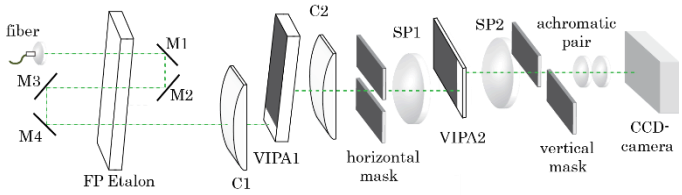

Figure 2.1 Setup of Brillouin spectrometer with Fabry-Perot etalon filter; the triple pass Fabry-Perot filter is built using a four mirrors configuration.

By changing the angle between the etalon and the incoming beam, the filter bandpass can be tuned with high precision to isolate the desired Brillouin scattering signal (Stokes peak from a water sample in this case), as shown in Figure 2.2. This allows to suppress the stray

laser light due to reflections within the spectrometer as well as the background noise due to elastic scattering within the sample.

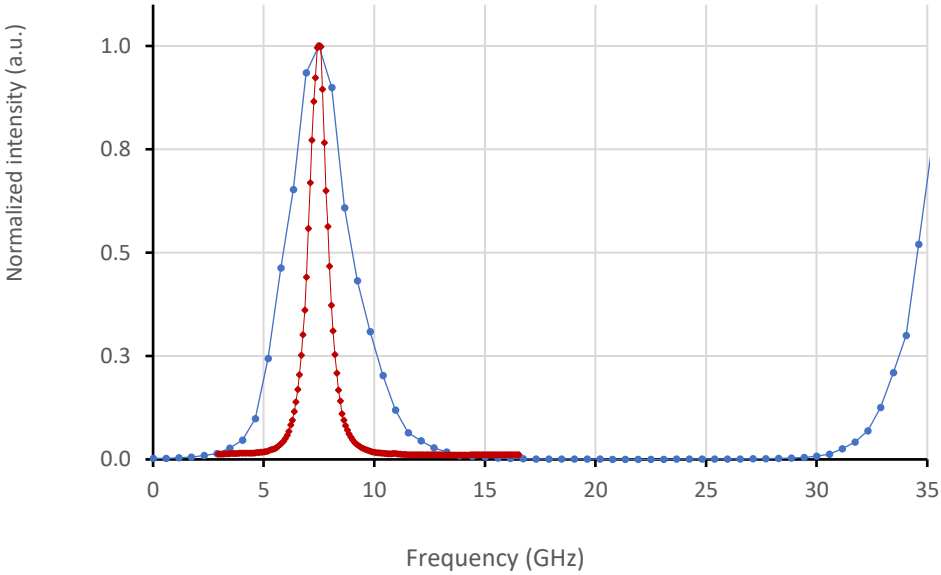

Figure 2.2 Bandwidth of 3PFP filter. We can observe a comparison between the 3PFP transmission profile and the Brillouin anti-Stokes signal of a water sample. The Stokes peak is suppressed by the 3PFP filter, while the anti-stokes is transmitted successfully.

Note that, in Figure 2.2, also the Brillouin Stokes component is suppressed. However, because typical variations within samples in Brillouin measurements are less than 2 GHz, the bandwidth of the filter is large enough to perform Brillouin imaging in one setting without the necessity of tuning the angle. The spectral extinction of the spectrometer is characterized in Figure 2.3. To construct the curve, we performed several measurements of the two-stage VIPA spectrometer extinction while varying the angle (and thus the central frequency) of the Fabry-Perot filter. Because the transmitted intensity varied over several orders of magnitude, the limited dynamic range of the camera could not capture the whole spectral profile in one setting; therefore, we acquired several profiles at fixed laser incident power in different detection configurations by tuning gain (g), exposure time (t), and using a neutral density filter of

throughput (f). The intensities (I) for each acquisition were then scaled according to the relation $I = \frac{counts}{g*t} * \frac{p}{f}$. The overall spectrometer has a maximum extinction of about 85 dB with optical throughput of 16% (58% from the 3PFP filter and 27% from the two-stage VIPA spectrometer). This is about 15 dB larger than previous spectrometers with similar throughput.6 Because the FSRs of the FP filter and of the VIPAs are not matched, the two VIPA peaks at 0 and 17 GHz do not have equal intensity, and the point of maximal extinction does not fall at half of the two VIPA peaks. If the FSRs of 3PFP and VIPA etalons were to be matched, the maximum extinction would be larger than 90 dB with the same overall throughput.

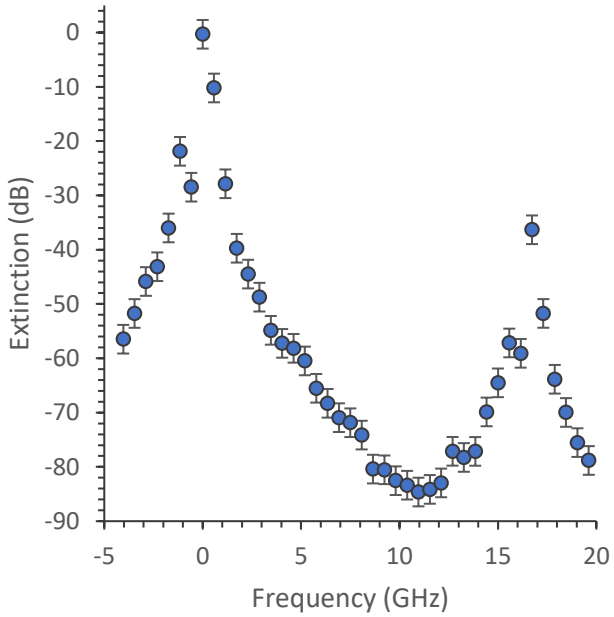

Figure 2.3 Extinction ratio of the VIPA Spectrometer with FP etalon filter. The VIPA spectrometer contribution to the overall extinction ratio (48dB) and the 3PFP contribution (36dB) contribute to the overall extinction (84db)

To quantify the performances of our setup in the measurements of turbid media, we connected the Brillouin spectrometer to an inverted confocal microscope and measured the

Brillouin spectra of intralipid solutions. Light from a 532 nm single mode laser was focused into an intralipid solution sample, placed in a transparent plastic dish. Figure 2.4(a) shows photographs of intralipid solutions of increasing concentration and increasing opacity. Intralipid solution at 10%, clearly non-transparent, is generally used to mimic the elastic scattering properties of biological tissue and thus provide a useful tool to quantify the rejection of non-Brillouin scattered light and compare it across studies. Previous works have shown that a two-stage VIPA spectrometer can suppress the elastic scattering component only up to a concentration of 0.001%; a three stage spectrometer can suppress the background light of up to a 5% Intralipid solution but with a total loss of over 90%.[40]

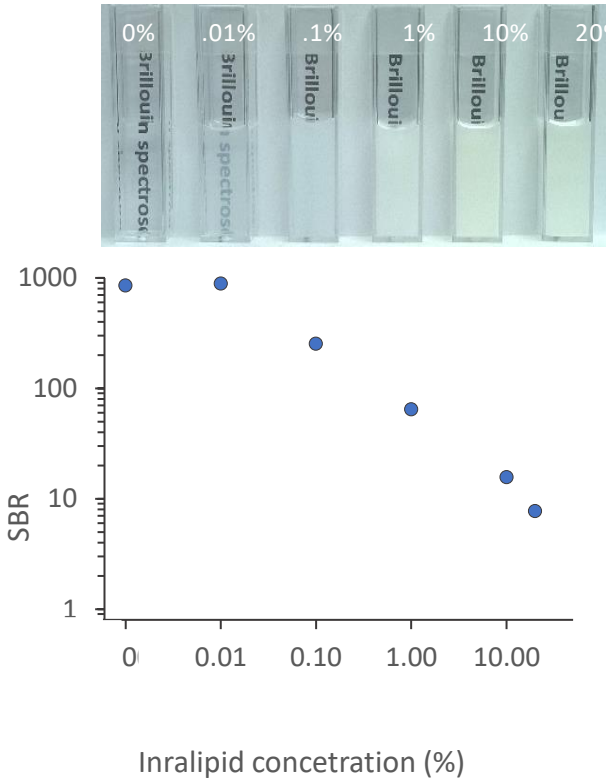

Figure 2.4 Measurements on Intralipid solutions; the values are calculated on 100 frames average. (a) qualitative comparison of transparency for different concentration. (b) Signal to background ratio for different Intralipid concentration.

Figure 2.3(b) shows the signal to background ratio (SBR) of a Brillouin spectrum acquired from pure water up to a 20% intralipid solution. The elastic background is very well suppressed, showing an SBR greater than one at all concentrations. Importantly, we verified that at 10% intralipid solution, our Brillouin measurement is shot-noise limited, thus unaffected by elastic background.

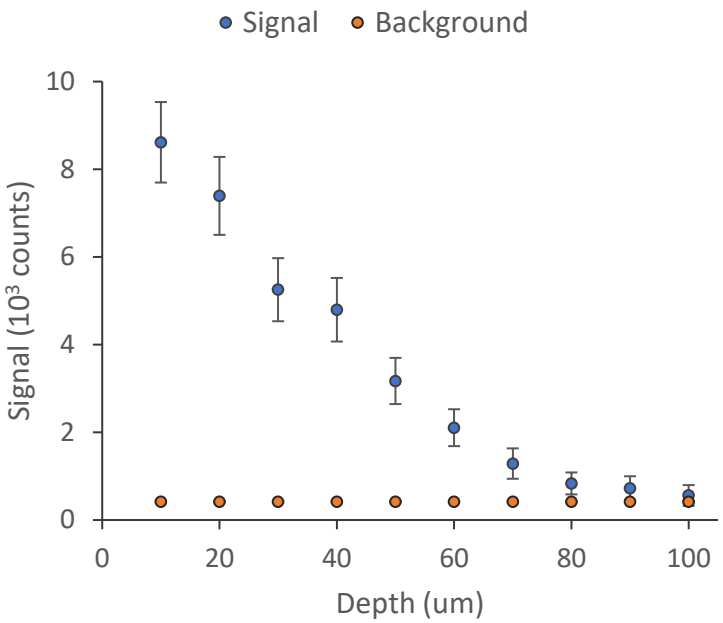

Figure 2.5 Comparison between Brillouin signal and elastic scattering light component at different depths.

Next, we demonstrated the ability to detect backgroundfree Brillouin signal from biological tissue. The tissue sample was a thin slice of chicken breast of area of about 1 cm2 , placed on the bottom of glass dish plate. The laser light was focused into the tissue through the glass cover-slip at a power of 6 mW and exposure time of 300 ms. Fig. 2.5 shows the Brillouin signal intensity as a function of tissue depth reported as average and standard deviation of 100 frames. The focusing depth was varied by translating the objective lens along the z-axis of the microscope. For comparison, the background signal at each depth is reported, showing the excellent suppression of the elastic scattering provided by the instrument. Figure 2.6 shows the signal to noise ratio (SNR) of this measurement as a function of tissue depth. Brillouin spectra with SNR greater than one were obtained from the tissue at depths up to 100

lm. We observed an exponential decay of SNR yielding a mean free path of 150 lm, consistent with the intensity loss due to elastic scattering in chicken breast tissue [55] and thus similar to other optical modalities that do not suffer from background issues.

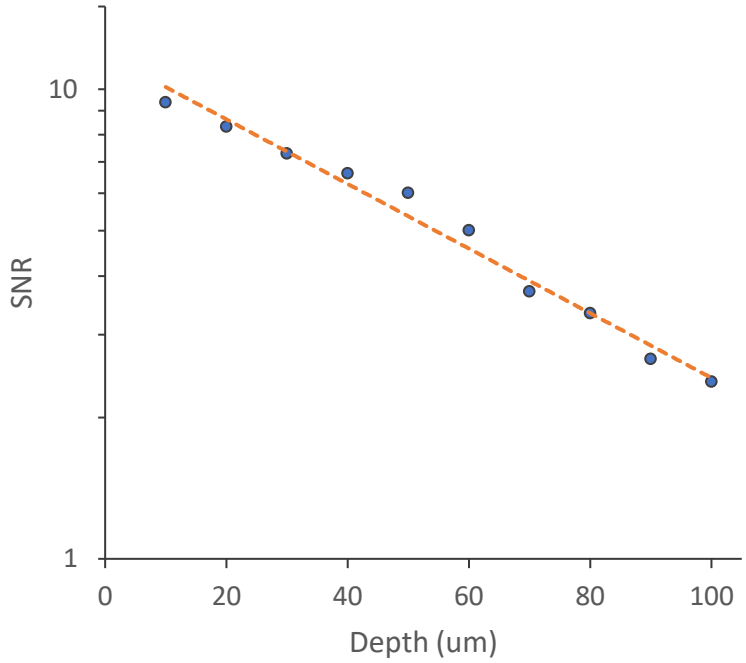

Figure 2.6 Signal to noise ratio as a function of depth; the SNR is calculated on 100 frames average, with an exposure time of 0.3s. The exponential fit leads to a mean free path of ~150 microns.

Importantly, other methods of rejecting elastically scattered light that use absorption lines of gas cells require experimentalists to perform Brillouin measurements with specific laser wavelengths and are prone to degradations due to laser frequency drift. In contrast, our spectrometer maintains its performance over a spectral band only limited by the coatings of the optical elements (Fabry-Perot, VIPA, mirrors, and lenses). Therefore, the spectrometer can accommodate Brillouin experiments with a wide variety of excitation wavelengths; moreover,

operating at low-finesse and with a tunable etalon, laser frequency drifts can be effectively handled.

Several improvements can be implemented to improve the practical performances of our spectrometer. As mentioned before, the FSR of the Fabry-Perot etalon and the VIPAs should be the same to reach maximal extinction. Moreover, using the same principles demonstrated here, a reflection configuration of the 3PFP would allow to build a notch-filter rather than a bandpass filter, with similar performances of throughput and extinction but larger transmitted bandwidth, which could be useful for Brillouin measurements exhibiting large shift variations of non-homogenous sample.

In conclusion, we have developed a two-stage VIPA Brillouin spectrometer with confocal sampling and a triple pass Fabry-Perot bandpass filter. We demonstrated rapid Brillouin measurement of intralipid solutions and turbid biological tissue with effective suppression of elastic scattering background. This investigation may expand the reach of Brillouin technology beyond ocular tissue to important areas such as the mechanical characterizations of tumors and atherosclerotic plaques.

2.3 Light recirculation in VIPA etalons

As mentioned in paragraph 1.2.2 a configuration featuring two VIPA etalons in cross-axis configuration since it offers an optimal compromise between insertion loss and spectral extinction: a standard two-stage VIPA spectrometer typically provides overall throughput of ~40%, finesse greater than 35 and extinction ratio of ~60 dB. Two-stage cross-axis VIPA spectrometers have witnessed constant development that greatly improved their performances, such as the addition of a third VIPA stage [40], apodization filters [43,56], etalon notch/bandpass filters [52,57], interferometric filters [], spectral coronography [59], gas cells [60-61], etc. However, the two-etalon configuration carries unresolved drawbacks such as the size, that can reach 1.8 m in length by 0.3 m in width when using typical 200 mm optics [42], as well as the need to have and align two VIPA etalons on different spatial axis. As a result, several attempts have been made to avoid a second etalon, maintaining the same level of performance [62-68]. Here we present a novel approach to the construction of a two stage VIPA spectrometer featuring only one VIPA etalon[2]; thanks to a beam folding design that relies on two polarized beam splitters and a beam steering element, light is dispersed on two orthogonal axes within the same etalon. We thus obtained a compact, single etalon spectrometer (0.5 by 0.4 meters) with performance equivalent to the standard implementation, and a footprint of about three-fold reduced in length and surface.

2.3.1 Working principle and experimental setup

A traditional two stage cross axis VIPA spectrometer (Fig. 2.7a) is designed so the light is independently dispersed on two spatial axes: the light is focused in the first etalon and the

[2] This section is based on a published peer-reviewed article [69]

output pattern is then focused on the orthogonal axis into a second etalon mounted perpendicularly to the first one. The resulting pattern is then imaged onto a CCD camera. Our goal was to recreate the same dispersions steps, while using and aligning a single VIPA etalon. In order to achieve this result, we designed a light folding architecture that allows the light to be dispersed twice by the same VIPA on two different spatial axes (Fig. 2.7b). The dispersion on the second dimension is accomplished by rotating the VIPA pattern at 90° and focusing it into the entrance of the VIPA a second time. Thus, the system results to be equivalent to a second VIPA oriented along the orthogonal axis with respect to the first one. Figure 1 shows how the classic and the single etalon folded implementation lead the input beam through the same dispersive steps; thus, the two system are expected to have same spectral performance, with the latter configuration to be preferred in terms of compactness, cost and ease of alignment.

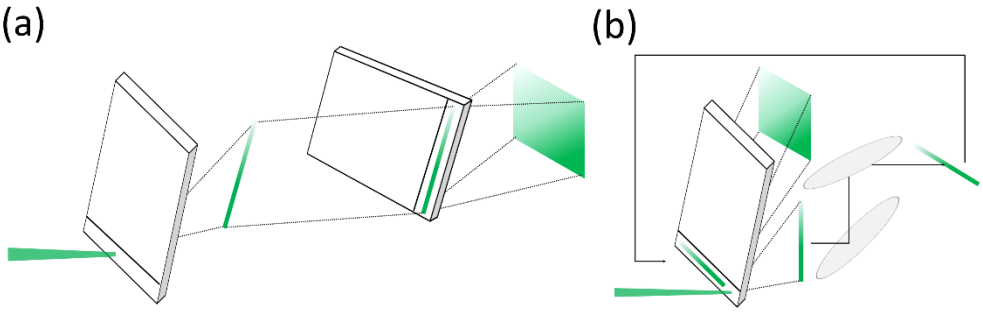

Figure 2.7 Principle of light recirculation in VIPA etalons. (a) 2-stage cross axis VIPA spectrometer in which light is dispersed on two spatial axis with two different etalons in cross axis configuration. (b) Single etalon cross axis VIPA spectroscopy principle; the output pattern from the first pass is rotated and recirculated through the same etalon.

In our experiment we used a 532nm CW laser (Laser Quantum, Torus-532) coupled into a single mode fiber as light source, and a VIPA etalon with free spectral range of 20 GHz

(Light Machinery) as dispersive element. In practice, the described system has been implemented as shown in figure 2.8: a half-wave plate (HWP1) at the output of a single mode fiber (SMF) orients the polarization of the beam on the parallel plane (SP-state). The beam is then focused by a cylindrical lens (C1), transmitted by the first polarized beam splitter (PBS1) and dispersed by the VIPA etalon; at this stage a second half-wave plate (HWP2) oriented perpendicularly to the first one changes the polarization to PS-state, allowing the beam to be reflected by the second polarized beam splitter (PBS2). The VIPA pattern is focused by a cylindrical lens (C2) in a 1-dimensional spatial filter (SLIT1). A spherical lens (S1) focuses the light into the VIPA for the second time, after being rotated by a beam steering system (BSS) and reflected by PBS1 thanks to its opposite polarization. Like in the first pass, the polarization is inverted back to P-state by the HWP2 so that the pattern can now pass through PBS2, be focused by a second spherical lens (S2) through the second slit (SLIT2), and imaged onto the CCD camera.

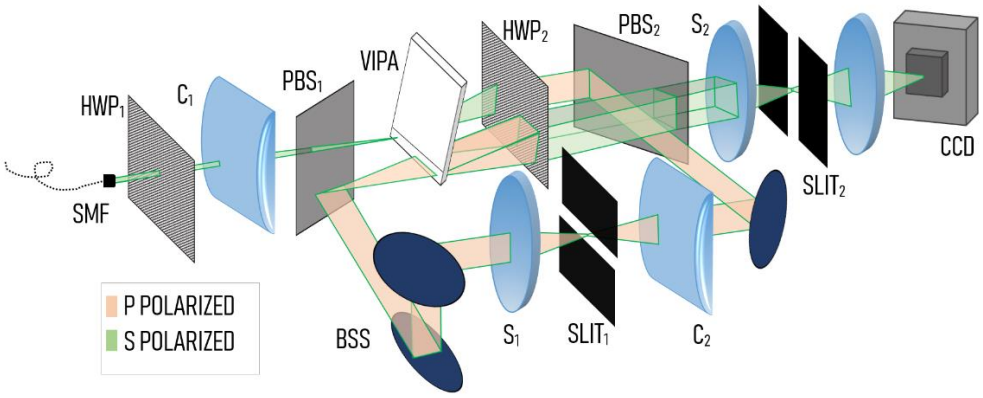

Figure 2.8 Experimental setup of a single etalon cross axis VIPA spectrometer. SMF: single mode fiber, HWP: half wave plate, C: cylindrical lens, f =200mm, S: spherical lens, f =200 mm, PBS: polarized beam splitter

Unlike a standard cross axis two-stage VIPA spectrometer, in this novel approach there is a single etalon that needs to be aligned with the first passing beam. The second pass beam is aligned to be perfectly parallel to the former, resulting in minimal or no VIPA adjustment required at the second stage. In order to align the to beams perfectly parallel we used the residual light reflected by PBS1 at first passage and transmitted at the second. The two weak beams have been aligned to be parallel at long distance, resulting in their stronger counterparts to be aligned as well. In case brighter beams are required, it is possible to adjust HWP1 so the alignment beams gradually gain intensity. In conclusion. we found the additional require optics elements such as PBS, HWP and BSS to be quicker to align and optimize than a second stage VIPA.

Perhaps, among the additional elements introduced in this configuration, BSS is the most sensitive; there are several ways to realize the pattern rotation, such as a two-mirrors beam steerer or a Dove prism oriented at 45°. In our demonstration we opted for the former since it is simpler to implement. It should be noticed how, to minimize cross talk between the two passes, the two light paths are not overlapped but rather parallel to each other. However, even though the beams are separated, for the sake of optimal performance, it is crucial that the incident angle in the VIPA of both beams is the same. As a result, not only the same interference order will be optimized on both dispersion axis, but it is also possible to tune both VIPA stages adjusting the tilt of the single etalon. In other words, the same entrance angle in the etalon ensures equal dispersive performance on both axes and allows one-touch fine tuning capability.

2.3.2 Results and discussion

In order to characterize our instrument, we measured the effective throughput and finesse as a function of the angle between the incoming beam and the VIPA etalon. Varying this angle changes the path of the light inside the etalon, modifying resulting interference pattern. Specifically, it is possible to adjust and optimize the entrance angle so that a specific interference order is preferred to the others in terms of throughput. As previously mentioned, if the two incident beams enter the VIPA with the same angle, the peak order will be the same on both axes. Thus, tuning the tilt of the VIPA will adjust both stages of the spectrometer. The results of this measurement are reported in Figure 2.9a, showing an optimal compromise between the third and the fourth order, with effective throughput around 18% and finesse of ~40. It is important to remark that the effective throughput is defined as total input power over power output of a single VIPA interference order, while the overall throughput expressed as total output power over total input power was 23% at peak performance. Experimentally, the measurement is performed by physically blocking all other orders with a slit, and placing a power meter right after the slit. This reflects the conditions in which Brillouin spectral measurements are usually configured, and therefore more descriptive of our instrument performance.

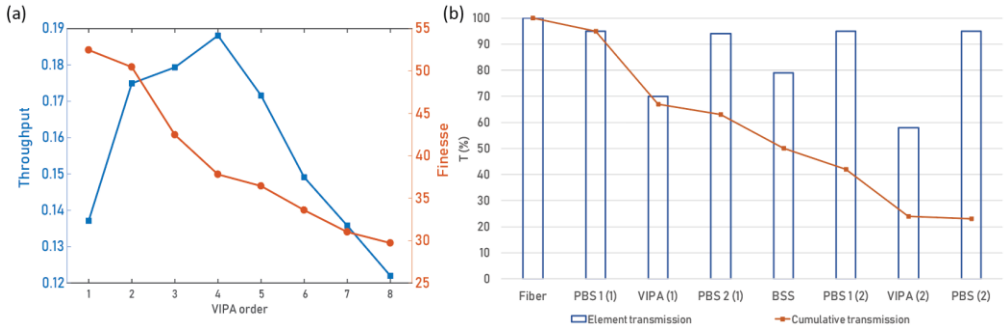

Figure 2.9 Single etalon spectrometer characterization. (a) Effective throughput and finesse performance as a function of the VIPA order. Effective throughput is measured as ratio between total power output at given order after two VIPA stages and the overall input power. Finesse is measured as spectral linewidth over free spectral range (FSR). (b) Step-by-step throughput characterization. Blue bars report the transmission efficiency of every element, the red line shows the overall throughput at every location. In parenthesis is expressed the iteration through a certain optical element.

In order to better characterize the losses, we performed a step-by-step analysis of the efficiency of all optical components, which is reported in Figure 2.9b. From this analysis, we concluded that our polarization switch system (PBS-HWP) has a relatively low efficiency (~95% per pass) which leads to an overall 20% loss over the required four passes. More efficient components or a mirror based recirculating system can greatly improve the throughput. Moreover, our beam steering also shows low efficiency performance (~80%) which we linked to the large size of the VIPA pattern compared to the mirror size. As a result, in ideal experimental conditions, we expect losses only due to the VIPA etalon, which in our case would mean an overall throughput of ~35%.

To evaluate the spectral performance of our instrument, we characterized the spectral linewidth and extinction ratio. Fitting the two-peak profile obtained on the CCD camera (fig. 2.10a) with a double Lorentzian function, we measured a linewidth of 0.48 GHz. Subsequently we measured the spectral contrast after the first and second stage. In order to quantify the

performance at the first stage we simply changed orientation of HWP2, letting the beam to be imaged on the CCD sensor without recirculation. In contrast, the second stage measurement has been performed with the recirculation enabled. The ability to visualize either one or two stage on the camera becomes crucial during the first alignment and characterization, thus it is worth mention it. As shown in fig. 2.10b our instrument reaches an extinction of ~58dB, comparable with a standard two stage cross axis spectrometer. It is important to remark that, while the bare architecture of two cascaded VIPA stages offer a spectral extinction of ~60dB, in practice other optical elements are used to improve the extinction ratio such as VIPA apodization, etalons, interferometric filters and spectral coronography, so that a contrast of 75-80 dB is easily achieved. The design proposed here remains compatible with most of the mentioned solutions; for instance, apodization filters can be placed after the two exit sides of the PBS2, while a coronography can be implemented before the CCD camera.

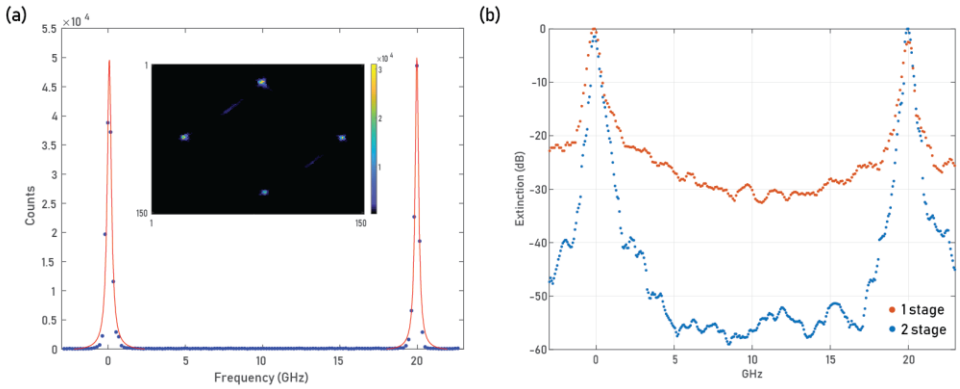

Figure 2.10 Spectral contrast of single etalon VIPA spectrometer (a) Camera frame and line plot of laser profile on the CCD camera. (b) Extinction ratio measurement of single stage and two stage VIPA spectrometer.

We have demonstrated a new implementation of a cross axis VIPA spectrometer in which the light is recirculated through the same etalon, obtaining overall throughput of ~23%,

finesse greater of ~40 and extinction ratio of ~58 dB. The throughput of the two VIPA stages is about 35%, a value compatible with standard two stage implementation; thus, the overall transmission efficiency performance can be greatly improved with high quality polarization management elements and larger beam steering mirrors; similarly, the spectral extinction can be improved with apodization and coronography filters. The footprint of our instrument is roughly three-fold smaller than previously reported instruments, with same focal length optics; this can be considered the main achievement of this optical design. In conclusions, our results show an equivalent performance to previous two-VIPA spectrometers, with advantages in terms of size, cost effectiveness and ease of alignment.

2.4 Single-axis VIPA spectroscopy

In the past, high spectral contrast has been accomplished by cascading multiple dispersive elements as well as implementing multiple passes through the same dispersive element. However, since this approach is limited to the sampling of a single frequency, it requires integration into spectral scanning devices, such as grating monochromators and Fabry-Perot scanning interferometers. Thus, the complete spectrum is obtained by sequential frequency scanning of single channels [34,70]. On the other hand, in instruments that can acquire an entire spectrum at once, also referred to as parallel or single-shot spectrometers, the cascade of dispersive elements has been achieved only in recent years in the so-called cross-axis configuration [41]. Such configuration offers much higher speed in spectra acquisition, but it remains severely limited in scalability because of degradations of the instrumental linewidth which directly affects the spectral resolution. As a result, spectrometers with high spectral contrast are typically slow in spectral analysis and processing [36], while fast spectrometers have limited spectral contrast [42].

In this section we discuss a novel approach to design spectrometers featuring a cascade of etalons which enables a high spectral contrast and rapid acquisition time without a significant compromise on the spectral resolution[3]. Differently from previous cascading approach, in our design, light is dispersed on a single geometrical axis, allowing for iterative multipass implementation on a single etalon. We experimentally demonstrate an implementation of this novel spectrometer design using VIPA etalons and performing Brillouin spectroscopy, an application where the weak inelastically scattered light component is extremely close (~0.01-0.001 nm) to much stronger spectral components, typically back-reflections and elastically scattered light. We selected VIPA etalons because of the immediate impact of our innovation to the biological applications of Brillouin spectroscopy where spectral contrast and acquisition time are of critical importance. However, the same optical design concept of single-axis cascading could be extended to other dispersive elements, such as diffraction gratings, echelle gratings or prisms.

2.4.1 Theoretical principle

The working principle of single-axis parallel spectroscopy is shown in Fig. 2.11: when an input beam hits the first spectral dispersion element, it is spatially separated into its spectral components along a certain dispersion axis. This set of spectral components are spatially separated, and thus can be more easily filtered or analyzed. In a traditional spectrometer, each component is independently isolated and quantified using a single channel passing filter such as a slit; this allows for a high spectral contrast at the expense of measurement speed. In a

[3] This section is based on a published peer-reviewed article [71]

parallel spectrometer the components are instead sent to a detector for the analysis of the whole spectrum.

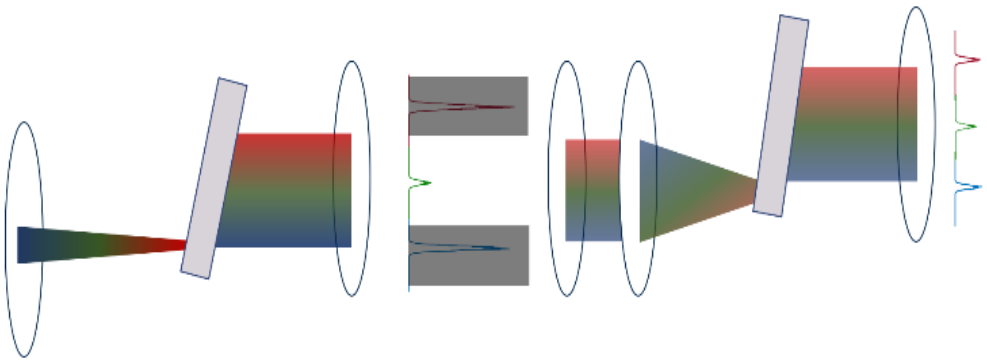

Figure 2.11 Working principle of etalon cascade on a single axis. Red and blue components represent unwanted spectral components, filtered by the mask. In green the signal frequency transmitted with optimized efficiency.

However, in experiments requiring high spectral contrast, the intensity of some of these components is so high that other components are not detectable even using a high dynamic range sensor. Here we show, that parallel spectral measurements are possible while filtering spectra like in scanning instruments by inserting suitable spectrum tailoring/filtering elements (such as masks, slits or apodizing filters) that decrease the intensity of unwanted frequencies in between dispersion stages [21,59,58]. The filtered spectrum is then reshuffled with a lens, and it enters a second spectral dispersive element where it is further split into its spectral components along the same dispersion axis by the second stage of the spectrometer. In this way, the portion of the spectrum that is not rejected by the spatial filter (i.e. green component in Fig. 2.11) is propagated through the multiple stages, and only attenuated by the effective throughput of the dispersive elements. On the other hand, spectral components that need to be attenuated (red and blue components in Fig. 2.11) are reduced in intensity by the product of

spectral extinction of the single dispersive elements and attenuation of the filtering elements. As the first stage in Fig. 2.11 reshuffles the light components into the second stage after the filtering element, the overall dispersive performances of the instrument are equivalent to the last stage, which operates as a single shot spectral measurement, while the spectral contrast of the instrument are highly increased by the previous stages, which act as high efficiency customized bandpass filters.

2.4.2 Experimental setup and its characterization

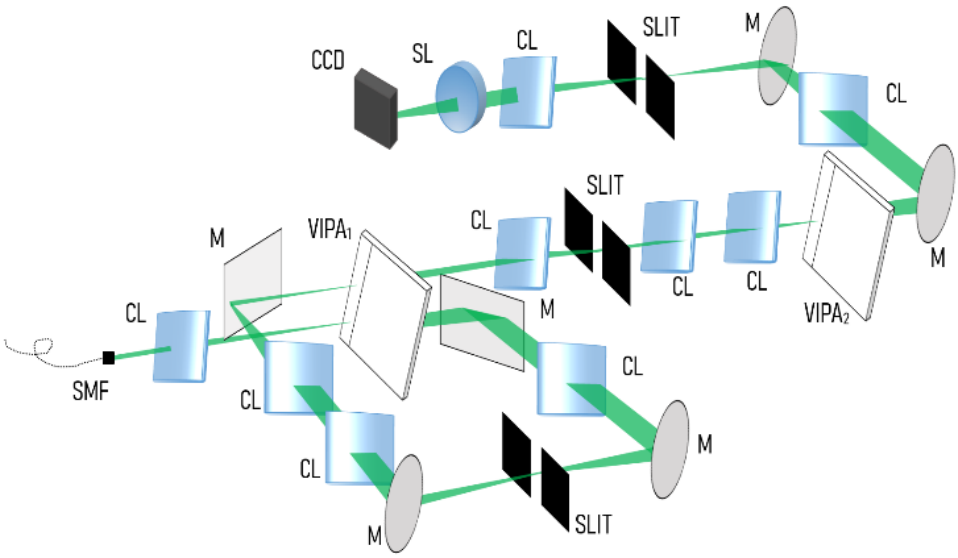

Figure 2.12 Setup of a triple-pass single axis VIPA spectrometer featuring two VIPA etalons.

The experimental setup is shown in Figure 2.12. To demonstrate the main features of our novel method, we have built a three-stage cascaded parallel VIPA spectrometer using two VIPA etalons; in our design, the first two stages feature two passes in the same etalon via recirculation [69], while a third dispersive element is cascaded downstream. Light output from a single mode fiber (SMF) is focused on the input window of a VIPA etalon which separates different spectral components at different angles; after the etalon, a cylindrical lens CL

transforms the angular separation into a spatial separation at its focal plane. Unwanted spectral components are then rejected through a slit acting a s spatial filter. A set of lenses images the plane of the slit onto the VIPA1 entrance window on a different point, to reduce cross talk. Since the spectral components of the light are recombined through the focusing lens before the entrance into the VIPA etalon, the dispersive elements should be selected to optimize specifications. Here, to efficiently detect Brillouin scattered photons of biological media, typically in the frequency range between 7.5 and 8.5GHz, we chose VIPA1 with a FSR of 17 GHz. This maximizes the distance between Brillouin signal and elastically scattered photons, which represent the noise. In this way cutting of the noise with the slit becomes straightforward. After the second dispersion, the light is filtered by a second spatial filter and subsequently focused into a second VIPA2 etalon, with FSR of 20GHz. Such value for the final etalon is chosen to have the best resolution in measuring a range on frequencies in the biological field. Therefore, we provided an example of a three-stage spectrometer in which the first two stages are optimized for background cleanup, while the last one is optimized for spectral frequency measurement.

For optimal performances, two parameters need to be considered at each etalon stage: 1) the incident angle into the etalon determines the finesse, as shallower angles enable a larger number of interference sources, but too shallow of an angle can clip the beam and decrease throughput. A typical compromise of these two quantities usually stands around 35 finesse and 75% throughput. 2) The numerical aperture into the etalon determines the range of angles inserted into the VIPA and thus how many diffraction orders are observed in the output. Usually, to maximize throughput, only one or two orders are desired.

Next, we analyze the performances of this experimental arrangement. At first, we evaluated the spectral extinction of the instrument. The measurement of such quantity involves the separate evaluation of the filtering stages and the dispersive ones. The contrast of the two filtering stages was measured using a power meter, resulting in 57dB of rejection. For this measurement, the filtering slit were engaged, blocking the unwanted signal as in a realistic measuring scenario. The dispersive stage spectral contrast was recorded with multiple spectral acquisition at different exposure time, to compensate the limited dynamic range of the EMCCD camera [3]. The overall extinction resulted to be ~79dB. This value is slightly under the theoretical maximum extinction of 90dB, which we ascribe to the imperfect coupling of light into the VIPA2 etalon due to reduction in beam quality from stage to stage. Importantly, this extinction value can be further improved with apodized etalons [56].

In terms of throughput, single-axis cascading resulted in ~10% overall throughput, which is better than previously reported cross-axis cascading methods [40]. Also, in terms of spectral resolution, this single-axis configuration is superior to cross-axis approaches. Since the same dispersion element can be used in both configurations, the ultimate performance will depend on the degradation of the single-stage instrumental linewidth. Cross-axis instruments have been shown to progressively distort the instrumental linewidth by a factor that depends on the rotation angle, with a reported spectral resolution of 0.6 GHz for two-stage instruments, and 0.7 GHz for three stages configurations [40]. In our case we measured a spectral resolution of ~0.52 GHz after three stages, demonstrating a significant improvement in instrumental linewidth degradation, comparable to single etalon performance. Such result is a direct consequence of the dispersion followed by spectrum reshuffling between every cascading

stage. In other words, the overall instrument provides the resolution of a single etalon approach (the last one in the cascade), while carrying the spectral extinction of three dispersive stages.

2.4.3 Results and discussion

We built a confocal microscope linked to the spectrometer via the SMF in order to characterize the performances of the spectrometer for Brillouin light scattering spectroscopy. We measured Brillouin spectra of water and methanol (Fig. 2.13). Since water and methanol have known Brillouin spectra, we also used these measurements to calibrate the spectrometer and verify its Free Spectral Range (FSR); we obtained FSR of 19.7Ghz, as expected matching the manufacturer specifications of VIPA2.

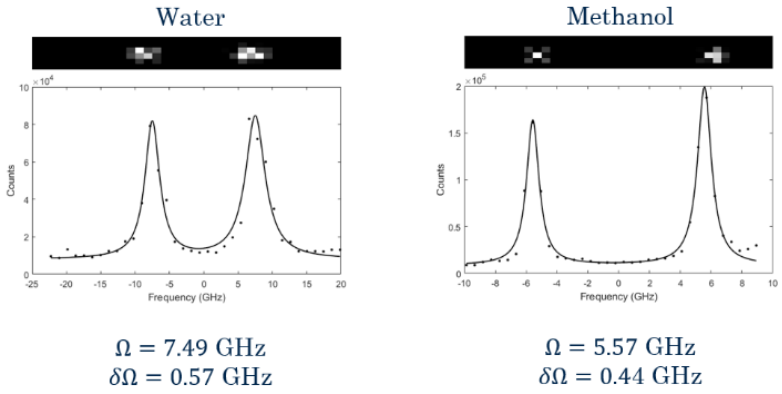

Figure 2.13 Single frames and averaged spectra (frames N=20) for two reference materials. The power used was 20mW, with 1s exposure time for water and 0.5s for Methanol. Measured Brillouin linewidth was respectively: 0.57 GHz for water and 0.44 GHz for Methanol.

To characterize the extinction properties of the spectrometer, we used intralipid tissue phantoms and measured the instrument signal to background ratio (Figure 2.14). As the sample becomes more turbid, the elastic scattering background is expected to increase making the Brillouin measurement more noisy. We were able to perform a measurement at 10% Intralipid concentration, which is representative of standard biological tissue [46] and obtained an SBR greater than 10. Such improvement when compared to instruments with a three etalon pass could be explained by the higher rejection of elastically scattered photons, which allows for better performance at such intralipid concentration.

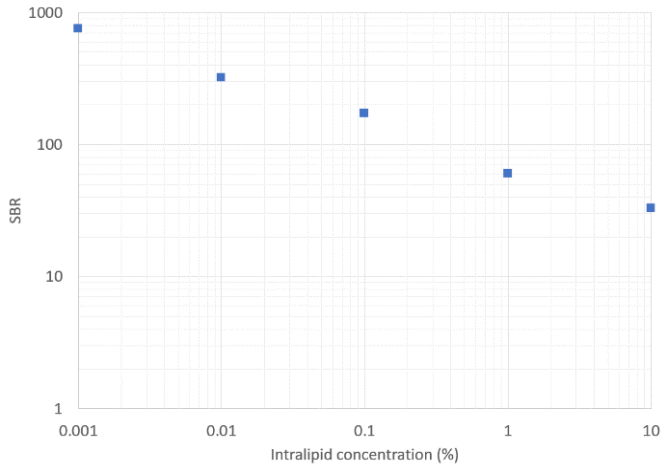

Figure 2.14 Signal-to-background ratio performance of a triple pass single axis VIPA spectrometer in Intralipid solutions.

Next, we quantified the parallel spectral bandwidth of the single-axis cascade spectrometer. By parallel spectral bandwidth, here, we define the range of spectral components that are measured/processed simultaneously by the spectrometer. To place this quantity into context, a parallel spectrometer has a large parallel spectral bandwidth, usually given by the free spectral range (FSR) of the dispersive element, and thus has a multiplexing factor equal to the finesse of the spectrometer (FSR/instrumental linewidth), typically above 30. In contrast, scanning spectrometers have parallel spectral bandwidth equal to the instrumental linewidth of the spectrometer, because they only transmit one spectral component at the time, i.e. a multiplexing factor of 1. Our scenario lies in between these two extremes: the parallel spectral bandwidth is less than etalon free spectral range (FSR), because it is also affected by the aperture of the filtering slit, and by the coupling of the beam focused into the VIPA etalons.

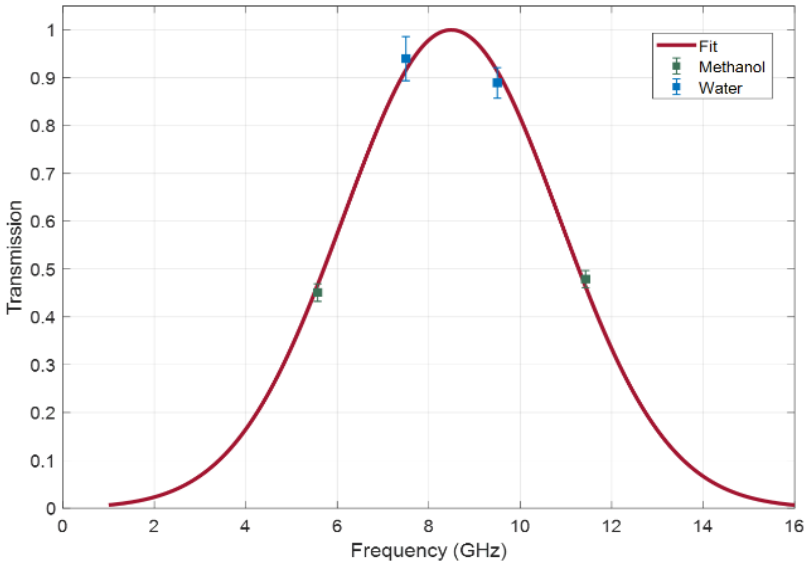

Figure 2.15 Frequency transmission of cascaded VIPA etalons. The water and methanol are used to fit a bandpass efficiency. Transmission of water signal results to be at T=0.9.

We experimentally quantified our parallel spectral bandwidth using water and methanol Brillouin spectra. The water-methanol relative intensity of the signal was calibrated on a

conventional cross-axis VIPA spectrometer, resulting to be approximately 1:3. Knowing the relative scattering intensity of the two materials, we could characterize the overall spectral attenuation due to the convolution of all contributing factors. The resulting curve (Fig 2.15) shows a bandwidth FWHM of 5.56 GHz. Considering the measured instrumental linewidth of 0.52 GHz, this yields a multiplexing factor of ~10. Importantly, this multiplexity is more than enough to perform parallel high-resolution Brillouin spectroscopy, as it is close to the limit imposed by Stokes and anti-Stokes signals of positive and negative spectral shifts.

In summary, the spectrometer described here offers a design alternative to multipass scanning etalons and parallel cross-axis cascades. Starting from this configuration, spectral performances can be further improved using previously demonstrated solutions such as apodization, interferometers, coronagraphy and atomic absorption filters. The performance demonstrated here has been obtained by using a filtering slit to cut the dominant and unwanted spectral lines, i.e. elastic scattering components, while letting the rest of the FSR through.

One critical design issue when considering single-axis cascading of multiple VIPA etalons is the matching of angles and numerical apertures at subsequent stages. In single etalon scenarios, or in two-stage cross-axis configurations, a gaussian collimated beam is used to input the etalon, which can be optimally adjusted as previously described. Instead, here, the VIPA pattern from a previous stage is the input into the entrance window of the next stage; this requires adjusting the input numerical aperture via sets of lenses and as a result the incident angle. We achieved a satisfactory operation point in this respect that is scalable to multiple stages as shown by the minimal linewidth degradation compared to single stage and the superior throughput to three-stage cross-axis configuration; however, the matching remains suboptimal compared to gaussian beam operation, which results in the excess insertion loss.

In conclusion we have shown a novel spectroscopy approach using the same dispersion axis in a cascade configuration. This results in a high-resolution etalon spectrometer with extinction performances close to scanning instrument and acquisition times close to parallel spectroscopy.

CHAPTER 3: DUAL-GEOMETRY BRILLOUIN MICROSCOPY FOR DIRECT 3D MAPPING OF REFRACTIVE INDEX

In this chapter we will present a novel Brillouin microscopy technique that probes the refractive index of materials relying on photon-phonon interactions, not optical path delays, and thus decouples optical from geometrical path[4]. The technology is based on measuring two inelastic Brillouin scattering interactions in confocal configuration, probing the same acoustic phonon axis so that the refractive index is the only physical quantity that affects the ratio of the two Brillouin frequency shifts. We experimentally demonstrate that using this dual photon-phonon scattering, the refractive index can be determined directly, with three-dimensional spatial resolution, accessing the sample from a single side and without assumptions on the geometrical dimensions of the sample.

3.1 Introduction to refractive index measurement

When light propagates inside a material, the phase of the electromagnetic wave is sensitive to the optical path, which fundamentally couples the geometrical path and the local index of refraction. Thus, methods to map the refractive index of a material (e.g. phase contrast microscopy [74,75], digital holography microscopy [76,77], optical coherence tomography [78,79], and more [80-83]) are intrinsically indirect as they rely on the knowledge, assumption, or measurement of the spatial dimensions of the sample. Even when optical path delay and thickness of the sample are well characterized, we can only obtain the average refractive index along the beam propagation axis. This fundamental issue has important practical ramifications as it prevents performing spatially-resolved measurements of the index of refraction. Mapping

[4] This chapter is based on a published peer-reviewed article [73]

the distribution and variations of the local refractive index is potentially crucial to analyze mass density behavior in cell biology [84,87], cancer pathogenesis [88,89], and corneal or lens refraction [90-92].

Several techniques in the past years have emerged to circumvent the coupling of geometrical path and refractive index in 3D samples using a tomographic approach, i.e. performing multiple measurements from different angles to reconstruct the internal refractive index distribution [93-97]. Tomographic phase microscopy enabled spatially-resolved measurements of refractive index for the first time. However, as the individual measurements are still based on optical path delay, known geometrical boundary conditions and/or reference refractive index values are needed as well as access to the sample from at least two sides. In addition, even under these conditions, the measurements are subject to artifacts due to phase wrapping when phase variations inside the sample are not smooth [74,75,86].

3.2 Phonon-photon scattering with complex refractive index

To better understand the light-matter interaction governing the phenomenon, we shall use the classical light scattering formalism [6,11]. This description links the scattered electric field $\mathbf{E_s}$ of wavevector $\mathbf{k}_s$ and frequency ω_s to the interaction of an incident electric field $\mathbf{E_i}$ of wavevector $\mathbf{k}_i$ and frequency ω_i with thermal-induced acoustic waves within a medium, which produce a dielectric constant variation in space and time. Let's start from the incident electric field:

$$\mathbf{E_i}(\mathbf{r}, t) = \mathbf{E_{i0}} e^{i(\mathbf{k_i}\cdot\mathbf{r}-\omega_i t)} + \text{c. c.} \tag{3.1}$$

where E_{i0} is the vector that expresses amplitude and polarization of the incident light and r is the scattering position vector. If this incident field encounters a fluctuation of the

dielectric constant, denoted by the tensor $\delta\varepsilon(r,t)$, the induced additional polarization in the medium will be given by

$$\mathbf{P}(\mathbf{r},t) = \frac{1}{4\pi}\delta\boldsymbol{\varepsilon}(\mathbf{r},t)\cdot\mathbf{E}_i(\mathbf{r},t) \tag{3.2}$$

And the resulting scattered electric field $\mathbf{E_s}$ can be obtained from Maxwell equations in dielectric media:

$$\nabla^2\mathbf{E_s} - \frac{1}{c^2}\frac{\partial^2\mathbf{E_s}}{\partial\, t^2} = \frac{1}{\varepsilon_0 c^2}\frac{\partial^2\mathbf{P}}{\partial\, t^2} \tag{3.3}$$

where ε_0 is the dielectric constant of vacuum, and c the speed of the electromagnetic radiation.

Thus, the additional polarization acts as a source term and dictates the emitted scattered light. This is a valid formalism for scattering phenomena in general; for acoustic phonons, the variation of the dielectric constant is induced by the acoustic displacement in the medium. The acoustic displacement u(r,t) within the medium obeys the wave equation [98]:

$$\frac{\partial^2\mathbf{u}}{\partial\, t^2} - \Gamma\nabla^2\frac{\partial\mathbf{u}}{\partial\, t} - v^2\nabla^2\mathbf{u} = 0 \tag{3.4}$$

where v is the speed of the acoustic wave and Γ is the attenuation parameter. A solution to Eq. (3.4) can be written as sum of spatial Fourier components of all the waves that contribute to u(r,t):

$$\mathbf{u}(\mathbf{r},\mathrm{t}) = \frac{1}{(2\pi)^{\frac{3}{2}}}\sum_{\mu}\int |\mathrm{d}\mathbf{q}|\ \mathbf{u}_{\mu}(\mathbf{q})\, \mathrm{e}^{-i(\mathbf{q}\cdot\mathbf{r}-\Omega_{\mu}(\mathbf{q})\mathrm{t})} + \mathrm{c.c.} \tag{3.5}$$

where q and Ω are the wavevector and the frequency of the acoustic wave. These quantities are related by the dispersion relationship $\Omega^2 = \mathrm{q}^2[\mathrm{v}(\hat{\mathbf{q}},\Omega)^2 - i\Omega\Gamma(\hat{\mathbf{q}},\Omega)]$.

The sum over μ in Eq. (3.5) expresses the superposition of acoustic waves oscillating along different axes. In homogenous liquid samples only longitudinal modes are sustained, while in a general solid material both longitudinal and transverse modes are present. However, since the oscillation axes are orthogonal to each other and linearly independent, we can consider a single oscillation axis and remove the sum without loss of generality. Here, we will focus only on the longitudinal modes, since they induce significantly more efficient light scattering [99]. Importantly, longitudinal modes only scatter light polarized perpendicularly to the scattering plane, which results in negligible depolarization for any scattering angle [98]. Thus, the polarization of the scattered field is the same as the incident field.

The acoustic displacement induces a strain in the material, which for longitudinal modes is proportional to the displacement gradient. The coupling between dielectric constant and the strain is expressed by the elasto-optic tensor p which links a certain δε(r,t) to the strain ∇u(r,t). The tensor p will depend on the mechanical properties of the medium, state of matter and thermodynamic conditions. The resulting variation in the dielectric constant tensor can thus be expressed as a function of the spatial Fourier components of the acoustic wave:

$$\delta\boldsymbol{\varepsilon}(\mathbf{r},\mathrm{t}) = -\frac{\varepsilon_0^2}{2(2\pi)^{\frac{3}{2}}}\int |\mathrm{d}\mathbf{q}|\ \mathbf{p}\,\nabla\mathbf{u}(\mathbf{q})\, \mathrm{e}^{-i(\mathbf{q}\cdot\mathbf{r}-\Omega(\mathbf{q})\mathrm{t})} + \mathrm{c.c.} \tag{3.6}$$

and the additional polarization can be explicitly written by plugging Eq. (3.6) into Eq. (3.2)

$$\mathbf{P}(\mathbf{r},t) = -\frac{\varepsilon_0^2}{8\pi}(2\pi)^{-\frac{3}{2}}\int |d\mathbf{q}|\left[\left(\mathbf{p}\nabla\mathbf{u}(\mathbf{q})\right)\mathbf{E_{i0}}e^{i[(\mathbf{k_i}-\mathbf{q})\cdot\mathbf{r}-(\omega_i-\Omega(\mathbf{q}))t]} + \left(\mathbf{p}\,\nabla\mathbf{u}(\mathbf{q})\right)^*\mathbf{E_{i0}}e^{i[(\mathbf{k_i}+\mathbf{q})\cdot\mathbf{r}-(\omega_i+\Omega(\mathbf{q}))t]}\right] + c.c. \quad (3.7)$$

This additional polarization in Eq. (3.7) represents the oscillating polarization source of Eq. (3.4), thus we observe that it will give rise to a scattered electric field oscillating with a frequency of $\omega_s = \omega_i \pm \mathbf{\Omega}$.

As the characteristic frequencies of thermal-induced acoustic fluctuations are orders of magnitude lower than optical frequencies, we can approximate $\Omega << \omega_i$; thus, we can consider the acoustic displacement a weak function of time with respect to the incident electric field, and we can write $\partial^2 P/\partial t^2 \sim P$.

Moreover, given the dispersion relationship $k=\omega n(\omega)/c$, we can also approximate $n(\omega_i) \approx n(\omega_s)$, $k_i \approx k_s$, and $|k_i - k_s| \approx 2k_i \sin(\theta/2)$, where θ is the scattering angle, i.e. the angle between k_i and k_s.

In these conditions, a solution to Eq. (3.3) for the scattered field is:

$$\mathbf{E_s}(\mathbf{r}',t) = -\left(\frac{\omega_i}{c}\right)^2 \hat{\mathbf{k}}_\mathbf{s} \times \left[\hat{\mathbf{k}}_\mathbf{s} \times \int \frac{\mathbf{P}(\mathbf{r},t')}{|\mathbf{r}'-\mathbf{r}|}\,|d\mathbf{r}|\right]_{t'=t-|\mathbf{r}'-\mathbf{r}|n/c} \quad (3.8)$$

where r' is the observation position vector and t' is the retarded time coordinate, i.e. the time at the observation point. The double vector product relates the scattered field polarization to the one of the incident field and the one of the acoustic waves. Specifically, if the observation position vector is much larger than the scattering position vector (i.e. $r' >> r$), it results $\hat{\mathbf{k}}_\mathbf{s} \approx (r' - r)/r'$.

Plugging Eq. (3.7) into Eq. (3.8) we obtain:

$$\mathbf{E_s}(\mathbf{r}',t) = \left(\frac{\omega_i}{c}\right)^2 \frac{\varepsilon_0^2}{4\pi r'} \frac{1}{(2\pi)^{\frac{3}{2}}} \hat{\mathbf{k}}_\mathbf{s} \times [\, \hat{\mathbf{k}}_\mathbf{s} \times \int |d\mathbf{q}| \left(\mathbf{p}\nabla\mathbf{u}(\mathbf{q})\right) \mathbf{E_{i0}} e^{i(\mathbf{k_s}\cdot\mathbf{r}' - (\omega_i - \Omega(\mathbf{q}))t)} \int |d\mathbf{r}| e^{i[(\mathbf{k_i}-\mathbf{k_s}-\mathbf{q})\cdot\mathbf{r}]} +$$
$$\hat{\mathbf{k}}_\mathbf{s} \times \int |d\mathbf{q}| \left(\mathbf{p}\nabla\mathbf{u}(\mathbf{q})\right)^* \mathbf{E_{i0}} e^{i(\mathbf{k_s}\cdot\mathbf{r}' - (\omega_i + \Omega(\mathbf{q}))t)} \int |d\mathbf{r}| e^{i[(\mathbf{k_i}-\mathbf{k_s}+\mathbf{q})\cdot\mathbf{r}]} \,] + c.c. \quad (3.9)$$

In the limit of no acoustic and optical attenuation, the quantity ($k_i - k_s \pm q$) is real and the integrals in |dr| corresponds to a delta function $\delta(k_i - k_s \pm q)$. This condition can be interpreted as a momentum conservation relation, and it allows to associate every observation position r' with a unique q wavevector. In the rest of the derivation, we study the electric field in the wavevector domain:

$$\mathbf{E_s}(\mathbf{q},t) = \left(\frac{\omega_i}{c}\right)^2 \frac{\varepsilon_0^2 (2\pi)^{\frac{3}{2}}}{4\pi r'} \hat{\mathbf{k}}_\mathbf{s} \times [\, \hat{\mathbf{k}}_\mathbf{s} \times e^{i(\mathbf{k_s}\cdot\mathbf{r}' - (\omega_i - \Omega)t)} \left(\mathbf{p}\nabla\mathbf{u}(\mathbf{q})\right) \mathbf{E_{i0}} \int |d\mathbf{r}| e^{i[(\mathbf{k_i}-\mathbf{k_s}-\mathbf{q})\cdot\mathbf{r}]} +$$
$$\hat{\mathbf{k}}_\mathbf{s} \times e^{i(\mathbf{k_s}\cdot\mathbf{r}' - (\omega_i + \Omega)t)} \left(\mathbf{p}\nabla\mathbf{u}(\mathbf{q})\right)^* \mathbf{E_{i0}} \int |d\mathbf{r}| e^{i[(\mathbf{k_i}-\mathbf{k_s}+\mathbf{q})\cdot\mathbf{r}]} \,] + c.c. \quad (3.10)$$

In practice, every material will present both optical and acoustic attenuations, which means that the quantity ($k_i - k_s \pm q$) is complex in the general scenario. This leads to a frequency spread of the scattered light for any given wavevector q. To consider this effect, we can write the complex dispersion relationships for both electromagnetic and acoustic waves. In an optically isotropic material (see Section 3.4.4 for anisotropic materials), the wavevector amplitude k is defined by the dispersion relationship:

$$k = \frac{\omega}{c} n = \frac{\omega}{c} [n_1(\omega) + i n_2(\omega)] \quad (3.11)$$

We can also rewrite the dispersion relationship for the acoustic wave [6]:

$$q = \frac{\Omega}{v(\hat{\mathbf{q}},\Omega)} + i \frac{\Gamma(\hat{\mathbf{q}},\Omega) q^2}{2v(\hat{\mathbf{q}},\Omega)} \quad (3.12)$$

Using these definitions, we can solve the integral in |dr| in Eq. (3.10) to obtain:

$$\mathbf{E_s}(\mathbf{q},t)=\left(\frac{\omega_i}{c}\right)^2\frac{\varepsilon_0^2(2\pi)^{\frac{3}{2}}}{i4\pi r'}\frac{e^{i(\mathbf{k_s}\cdot\mathbf{r}'-(\omega_i-\Omega)t)}\hat{\mathbf{k}}_\mathbf{s}\times\left[\hat{\mathbf{k}}_\mathbf{s}\times\mathbf{p}\,\nabla\mathbf{u}(\mathbf{q})\mathbf{E_{i0}}e^{i(\mathbf{k_i}-\mathbf{k_s}-\mathbf{q})\cdot\mathbf{r}}\right]}{\left(\frac{2n_1\omega_i}{c}\sin\left(\frac{\theta}{2}\right)+\frac{\Omega}{v(\hat{\mathbf{q}},\Omega)}\right)+i\left(\frac{2n_2\omega_i}{c}\sin\left(\frac{\theta}{2}\right)+\frac{\Gamma(\hat{\mathbf{q}},\Omega)q^2}{2v(\hat{\mathbf{q}},\Omega)}\right)}+$$

$$\left(\frac{\omega_i}{c}\right)^2\frac{\varepsilon_0^2(2\pi)^{\frac{3}{2}}}{i4\pi r'}\frac{e^{i(\mathbf{k_s}\cdot\mathbf{r}'-(\omega_i+\Omega)t)}\hat{\mathbf{k}}_\mathbf{s}\times\left[\hat{\mathbf{k}}_\mathbf{s}\times\left(\mathbf{p}\nabla\mathbf{u}(\mathbf{q})\right)^*\mathbf{E_{i0}}e^{i(\mathbf{k_i}-\mathbf{k_s}+\mathbf{q})\cdot\mathbf{r}}\right]}{\left(\frac{2n_1\omega_i}{c}\sin\left(\frac{\theta}{2}\right)-\frac{\Omega}{v(\hat{\mathbf{q}},\Omega)}\right)+i\left(\frac{2n_2\omega_i}{c}\sin\left(\frac{\theta}{2}\right)-\frac{\Gamma(\hat{\mathbf{q}},\Omega)q^2}{2v(\hat{\mathbf{q}},\Omega)}\right)}+\text{c.c.}\qquad(3.13)$$

As expected, the scattered electric field oscillates with the same frequency of the polarization source frequency, $\omega_s = \omega_i \pm \Omega$. It should be noted that the difference in frequency between the incident and the scattered light corresponds to the frequency of the acoustic wave. For this reason, this result can be interpreted as an energy conservation relation.

We can obtain an expression for the frequency of the phonon as function of incident frequency (ω_i), scattering geometry (θ) and properties of the material, i.e. refractive index (n) and speed of sound (v):

$$\Omega=\mathrm{Re}(q)v(\hat{\mathbf{q}},\Omega)=2\frac{\omega_i}{c}n_1(\omega_i)v(\hat{\mathbf{q}},\Omega)\sin\frac{\theta}{2}\qquad(3.14)$$

We can now calculate the power spectrum of the scattered light using the Wiener-Kintchin theorem:

$$S(\mathbf{q},\omega)=\frac{1}{2\pi\langle|\mathbf{E_s}(\mathbf{q},t)|^2\rangle}\int_{-\infty}^{+\infty}d\tau\langle\mathbf{E_s}(\mathbf{q},t+\tau)\mathbf{E_s^*}(\mathbf{q},t)\rangle\,e^{i\omega\tau}\qquad(3.15)$$

Plugging equations (3.13) and (3.14) into Eq. (3.15), we obtain

$$S(\mathbf{q},\omega)\propto\left[\frac{\Gamma(\hat{\mathbf{q}},\Omega)q^2/2+n_2\Omega/n_1}{[\omega-(\omega_i-\Omega)]^2+[\Gamma(\hat{\mathbf{q}},\Omega)q^2/2\ +n_2\Omega/n_1]^2}+\frac{\Gamma(\hat{\mathbf{q}},\Omega)q^2/2+n_2\Omega/n_1}{[\omega-(\omega_i+\Omega)]^2+[\Gamma(\hat{\mathbf{q}},\Omega)q^2/2+n_2\Omega/n_1]^2}\right](3.16)$$

Equation (3.16) is the main result of the derivation showing the complete expression of the Brillouin spectrum featuring Lorentzian functional forms. Focusing on the center frequencies of the spectral peaks, we can observe two components symmetric with respect to the incident frequency (Stokes and anti-Stokes), and shifted by ±Ω. The linewidth of the Lorentzian function results to be

$$\Delta\Omega = \Gamma(\hat{\mathbf{q}}, \Omega)q^2 + 2\Omega\frac{n_2}{n_1} \tag{3.17}$$

Where we observe that the linewidth of the Lorentzian spectrum proportional to the attenuation coefficients of both electromagnetic and acoustic wave. In most general case, both these terms can contribute to the natural linewidth of the Brillouin signal.

3.3 Direct measurement of refractive index

3.3.1 Methods and experimental setup

In our method, we use two scattering geometries: 1) back-scattering, with incident and scattered photons normal to the sample interface, (0-geometry, Fig. 3.1a); 2) symmetric angled configuration with incident and scattered photons at an angle α with the sample interface (α-geometry, Fig. 3.1b).

Assuming negligible acoustic dispersion in the Brillouin frequency range, the frequency shifts for these geometries can be written as:

$$\Omega_0 = \omega_i\frac{2n_1(\omega_i)v(\hat{\mathbf{q}}_\mathbf{0})}{c} \tag{3.18}$$

$$\Omega_\alpha = \omega_i\frac{2n_1(\omega_i)v(\hat{\mathbf{q}}_{\boldsymbol{\alpha}})}{c}\left(1 - \frac{\sin^2\alpha}{n_1^2(\omega_i)}\right)^{\frac{1}{2}} \tag{3.19}$$

As shown in Fig. 1, these configurations probe the same phonon axis, i.e. $\hat{\mathbf{q}}_{\mathbf{0}} = \hat{\mathbf{q}}_{\boldsymbol{\alpha}} \equiv \hat{\mathbf{q}}$. Thus, defining $R=\Omega_\alpha/\Omega_0$ as the ratio between frequency shifts, we can derive the following expression for the local index of refraction:

$$n_1(\omega_i) = \left(\frac{\sin^2 \alpha}{1 - R^2}\right)^{\frac{1}{2}} \tag{3.20}$$

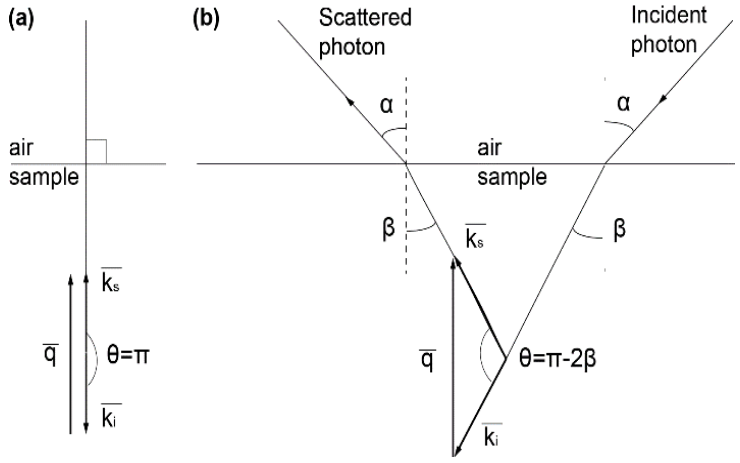

Figure 3.1 Dual-geometry phonon-photon scattering (a) 0-geometry configuration; (b) α-geometry configuration. Both geometries sample the same acoustic phonon direction inside the volume of interaction.

In Eq. (3.20), the dependence on other quantities of Eq. (3.14) is lost because the wavelength and the local index of refraction are the same for both geometries, and the speed of the phonon is the same in both configurations, as it is sampled along a common axis. Therefore, the ratio between the two Brillouin shifts depends only on the local index of refraction of the sample inside the scattering volume of interaction. Since no other physical quantity influences the measurement, this can be considered a direct measurement of the refractive index.

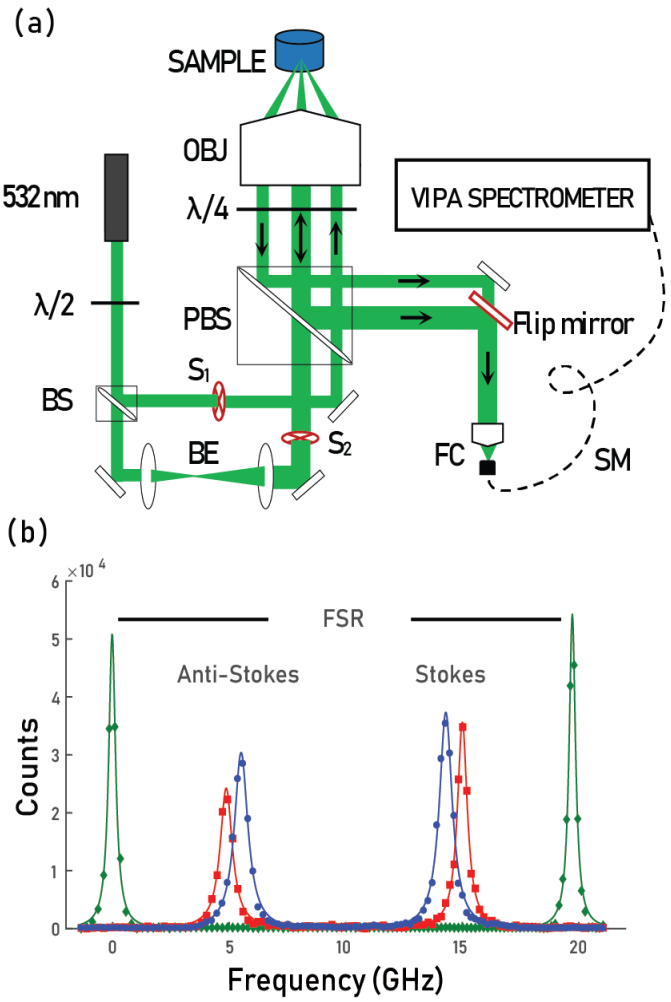

Figure 3.2 (a) Schematic of the dual-geometry Brillouin spectroscopy setup. A flip mirror and two shutters (S1, S2) work in alternate configuration to allow acquisition of the two scattering geometries. (b) Methanol spectrum for 0-geometry (blue) and α-geometry (red); the Rayleigh scattering peak (green) shows the free spectral range (FSR) of the etalon. Experimental data (dots) are fitted to a double Lorentzian curve (solid line) in MATLAB.

To demonstrate our method, we built the experimental setup in Fig. 3.2a; a 532nm continuous wave laser is split in two beams of different diameter: 5.4mm and 1.8mm. The incident beams are both focused into the sample through a dry 20x 0.75NA objective lens. The first beam is on the optical axis, i.e. at 0° incidence angle and its corresponding scattered light

is also collected on the optical axis. The second incident beam is off-axis at 5.5mm from the center of the lens at an angle α=37° and its corresponding scattered light is collected symmetrically at the same angle α. The scattered light for both geometries is coupled into the same single mode optical fiber acting as confocal pinhole, thus collecting light only from a microscopic 3D region within the sample. Three-dimensional mapping is achieved through a translational stage (Prior Scientific, ProScan II), that scans the sample all directions. This solution allows for 100 nm scanning resolution. Similar result could be achieved by scanning the beams through galvanometric mirrors. Such solution would imply a significatively lower inertia in moving component which translates in higher scanning accuracy and speed. However such solution would require higher complexity in alignment in order to preserve the angle between the two beams. Thus, we opted for a sample scanning approach. To facilitate collection of scattered photons from the proper scattering geometry, the two beams are alternated by a system of two shutters and a flip mirror (Fig. 3.2a). It would be technically straightforward to perform simultaneous measurements with two couplers and two spectrometers, or a parallelized spectral measurement [100]. A representative set of spectra for both geometries is shown in Fig. 3.2b.

To measure the small frequency shift due to photon-phonon interaction we built a double-stage VIPA spectrometer with ~0.7 GHz linewidth and 6 dB insertion losses. The VIPA etalon is conceptually like a Fabry-Perot etalon but has a front surface with a highly reflective coating and a narrow stripe anti-reflection coated to enable light input. Tilting the etalon enables single shot spectral measurements with acquisition times in the order of 0.1-1s. By scanning the sample with a translational stage and measuring two spectra at each location, the refractive index is mapped with 3D resolution. However, because of the different

illumination/collection paths [101], the voxels sampled by the two geometries do not fully overlap. The different voxel size worsens the effective resolution of the measurement which we define as the smallest region of homogeneous refractive index required to obtain a measurement without artifacts. In our configuration, the 0-geometry has a voxel of 1.31 x 1.31 x 33 μm; the α-geometry at an angle of ~37° has a voxel of 5.3 x 3.9 x 5.7 μm. Thus, our overall resolution is 5.3 μm x 3.9 μm (lateral) x 33 μm (axial). Improvements in spatial resolution can be achieved with different beam diameter and objective lens configurations.

3.3.2 Results and discussion

We validated our index of refraction measurement against gold-standard Abbe refractometry. We prepared several solutions of water and sodium chloride (NaCl) from pure water to the saturation point. All solutions were prepared and tested at constant temperature of 22 °C. The different salt concentration induces a variation of the refractive index from 1.33 to 1.39. Our method is highly consistent with the gold standard as the correlation is linear, the slope is ~1 with R^2>0.99 (Fig. 3.3).

To demonstrate our 3D mapping capability, we fabricated a non-symmetric sample using a drop of cured optical glue (Thorlabs, NOA61, n=1.56), deposited on a glass-bottom petri dish and surrounded by methanol (ThermoFisher, n=1.329). The result of our refractive index mapping of XY and XZ sections are in Figure 3.4. For this image, we used 15 mW incident power, and acquisition time 1 and 3s for backscattering and α-angle geometry, respectively. Despite the high asymmetry along the z-axis, we obtained accurate values for the index of refraction and we reliably reconstructed the dome profile of the deposited drop. A sample like this would be difficult to characterize for techniques based on optical path delay, in particular without access to the sample from two sides.

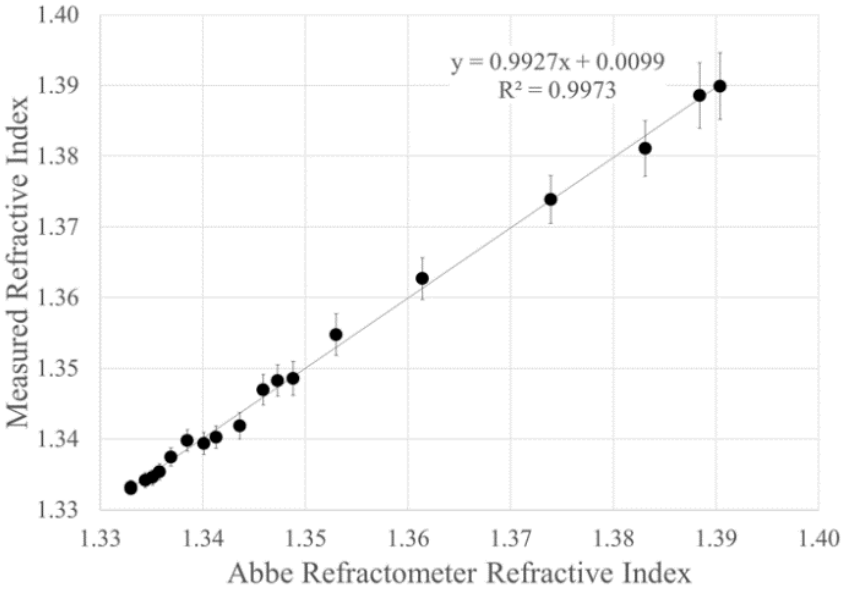

Figure 3.3 Measured refractive index for different water-NaCl solutions compared with Abbe refractometer's values. The larger error at high salt concentration is due to Brillouin peak broadening that affects the accuracy of the fit.

Interestingly, the co-localized Brillouin interaction can provide information also about the speed of the acoustic wave and the imaginary part of the refractive index. Indeed, from Eq. (8), the linewidth of the Lorentzian peaks is proportional to the attenuation coefficients of electro-magnetic and acoustic waves. In a material with no optical absorption, the linewidth is given by Γq^2, i.e. the inverse of the phonon lifetime; with strong optical absorption, the electric field amplitude decreases exponentially so that the imaginary part of the refractive index is dominant [102]. In the general case, both terms contribute to the linewidth of the spectrum; with our dual scattering geometry, the two terms can be independently measured if the spectrometer has sufficient spectral resolution.

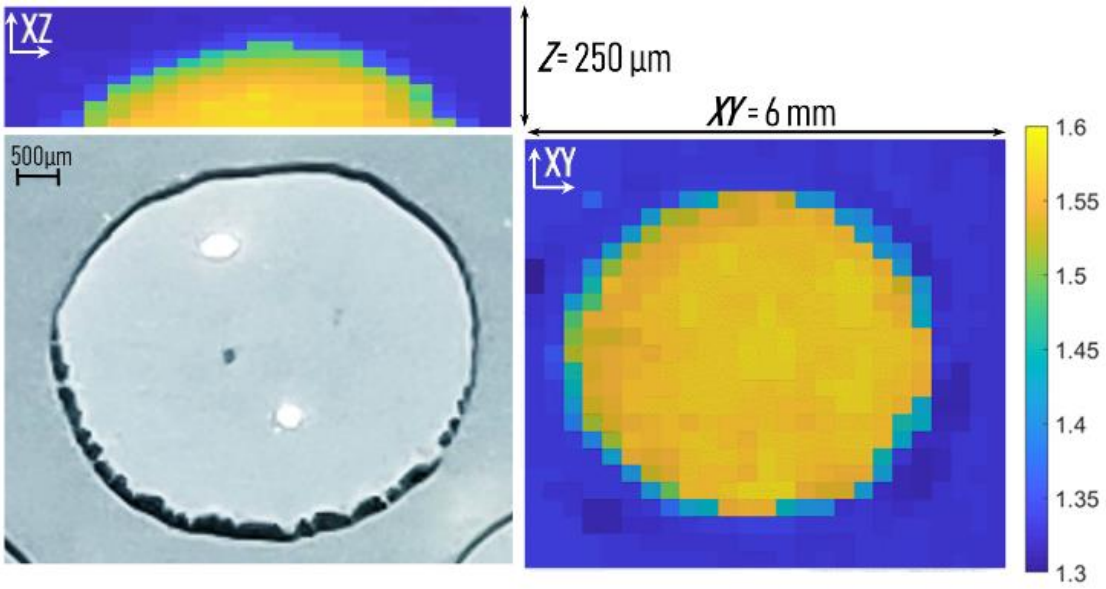

Figure 3.4 XY and XZ cross sections of a drop of photo-activated polymer (n=1.56) surrounded by methanol (n=1.329). Bright field image is also reported for visual comparison.

3.4 Considerations on experimental method

3.4.1 Spatial resolution

In the calculation of optical resolution, we need to take into account the resolution of both 0- and α-geometry. Indeed, as the voxels of the two configurations do not fully overlap, we define the effective resolution of the system on a given axis as the worst of the resolution between the two geometries. In confocal configuration, the spatial resolution for the 0-geometry is given by:

$$d_{x,y} = \frac{0.37\lambda}{NA_0} \qquad d_z = \frac{1.4\lambda}{NA_0^2} \tag{3.21}$$

Meanwhile, the spatial resolution of the α-geometry is given by the following expressions [101]:

$$d_x = \frac{0.37\lambda}{NA_\alpha \cos\alpha} \qquad d_y = \frac{0.37\lambda}{NA_\alpha} \qquad d_z = \frac{0.37\lambda}{NA_\alpha \sin\alpha} \tag{3.22}$$

The NA for each geometry is the effective numerical aperture given a certain objective lens and input beam diameter, α is the angle between the incident and collecting directions, and λ is the wavelength of the laser. Given these expressions, it is possible to calculate the voxel dimension on each axis for a range of configurations. The resolution of the system will depend on the objective lens used, diameter of the beams, and the maximum angle α that the objective allows. For the following simulation we used the angle α=37° used in our experiment, close to the maximum allowed by our current objective lens (0.75NA, 20x, Olympus).

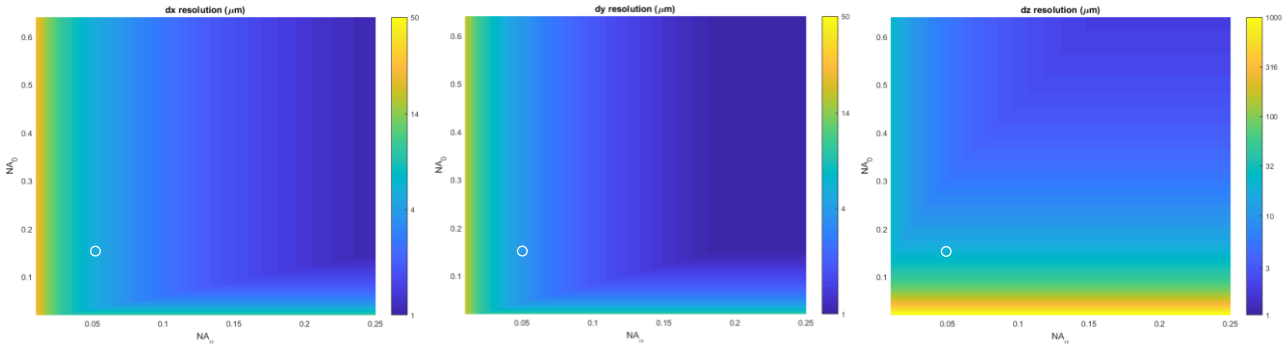

Figure 3.5 Overall resolution along the three spatial directions as a function of effective NAs of the two geometries. The white circle indicates the conditions of our current proof-of-principle experiment.

From figure 3.5 it is straightforward to see that high resolution is possible with this method. For example, for NA_0 =0.6 and NA_α =0.2, the effective voxel of the dual geometry system is 1.31 x 0.96 x 1.95 μm. Exploring different angle configuration and objective lens may allow a sub-micron resolution to be achieved on all axis.

3.4.2 Uncertainty on refractive index

In this section we derive the error on the index of refraction. For the sake of simplicity, we omit the subscript 1 to denote the fact we are considering the real part of the refractive index. From equation 3.20, it is possible to write the expression for the index of refraction as

a function of R, the ratio of Brillouin frequency shifts measured in the two-configuration described:

$$n = \sqrt{\frac{\sin^2 \alpha}{1 - R^2}} \tag{3.23}$$

Differentiating this expression, one gets:

$$dn = \frac{Rn^3}{\sin^2 \alpha}\, dR \tag{3.24}$$

The relative error on R can be written as:

$$\frac{dR}{R} = \sqrt{\frac{d\Omega_\alpha^2}{\Omega_\alpha^2} + \frac{d\Omega_0^2}{\Omega_0^2}} \tag{3.25}$$

Assuming $d\Omega_\alpha \approx d\Omega_0$, and knowing that $\Omega_0 = R\Omega_\alpha$, we obtain

$$\frac{dR}{R} = \sqrt{\frac{d\Omega}{\Omega_\alpha^2} + \frac{d\Omega}{(R\Omega_\alpha)^2}} = \sqrt{\frac{(1 + R^2)d\Omega^2}{(R\Omega_\alpha)^2}} = \sqrt{(1 + R^2)}\, \frac{d\Omega}{R\Omega_\alpha} \tag{3.26}$$

From the last formula, we get an expression for dR:

$$dR = \frac{\sqrt{(1 + R^2)}}{\Omega_\alpha}\, d\Omega \tag{3.27}$$

Plugging the latter in Eq. (3.20), we get the error on the index of refraction as a function of the error on the Brillouin frequency shift:

$$dn = \frac{Rn^3}{\sin^2 \alpha}\, \frac{\sqrt{(1 + R^2)}}{\Omega_\alpha}\, d\Omega \tag{3.28}$$

For reference, at λ=532 nm and α=37°, the shift of water is about 6.7 GHz, and R≈0.9. Plugging these values in Eq. 3.28, we find that in order to achieve an accuracy of 0.001 for index of refraction, it is necessary to determine the Brillouin frequency shift with an uncertainty better than 2.4 MHz. Since our instrument works in shot noise limited conditions, we adjusted the exposure time to match the desired accuracy. Alternatively, one could increase the laser power focused into the sample, increase the CCD camera gain, or select a wavelength with a higher scattering efficiency.

3.4.3 Correction factor for immersion objective lens

A correction term needs to be applied to the previous calculation in Eq. 3.20 in the case an immersion medium is used on the objective lens. Given n_{1_IM} the index of refraction of the media surrounding the objective lens, the sine of the angle $\theta/2$ can be expressed as

$$\sin\frac{\theta}{2} = \sin\left(\frac{\pi}{2} - \beta\right) = \cos\beta = \sqrt{1 - \sin^2\beta} = \sqrt{1 - \frac{n_{1-IM}^2 \sin^2\alpha}{n^2}} \tag{3.29}$$

As a result, Eq. 3.20 becomes:

$$n_1^2 = \frac{n_{1-IM}^2 \sin^2\alpha}{1 - R^2} \tag{3.30}$$

In our case n_{IM} is the index of refraction of the air, while for immersion objectives, the reference value of the immersion medium needs to go into the equation. More in general, one can consider the quantity $n_{1\text{-}IM}\sin(\alpha)$ as the sine of the equivalent angle of incidence in vacuum: $\sin(\alpha_{vac}) = n_{1\text{-}IM}\sin(\alpha)$. Thus, when using an immersion objective lens, a similar correction using $\sin(\alpha_{vac})$ instead of $\sin(\alpha)$ should also be applied.

3.4.4 Measurement in birefringent materials

In this section we will discuss implementation of dual geometry phonon-photon scattering approach for measurement of the real part index of refraction in optically anisotropic materials. For the sake of simplicity, we will omit the subscript 1 to denote the real part, as done previously. Let's consider the most common case of optical anisotropy: a birefringent material in which there is a single optic axis (uniaxial case). In the general case unpolarized incident light would be split in two components, one with polarization orthogonal to the optic axis, one with polarization parallel to it. The two components would respectively sense the ordinary (n_{ord}) and the extraordinary refractive index (n_{ext}). If we consider linearly polarized light with an arbitrary polarization direction, the sensed index of refraction n will obey the following relationship [103]:

$$\frac{n^2}{n_{ord}^2}\sin^2\psi + \frac{n^2}{n_{ord}^2}\cos^2\psi\cos^2\varphi + \frac{n^2}{n_{ext}^2}\cos^2\psi\sin^2\varphi = 1 \qquad (3.31)$$

Where ψ is the angle between the polarization direction of the light and the optic axis, and φ is the angle between the direction of propagation and the optic axis. Let's consider an experimental setup analogous to the one presented in Fig. 1 of the main text, in which two incident beams are focused on the sample; one of them is perpendicular to the surface ($\mathbf{k}_{i0}$), while the other one has an incident angle $\alpha \approx 37°$ ($\mathbf{k}_{i\alpha}$). The scattered light is collected on the same path for the former beam ($\mathbf{k}_{s0}$), and on a symmetric angle with respect to the normal for the latter ($\mathbf{k}_{s\alpha}$). These four vectors lie on a geometric plane that we will call scattering plane. The polarization of the light in all cases will be orthogonal to the scattering plane, according to the results from Eq. (S13). Thus, in the most general case the two scattering geometries will sense a different refractive index, that we can call respectively n_0 and n_α. These indexes will

depend on the optic axis orientation with respect to the scattering plane, as well as to the polarization of the light. Eqs. (3.18) and (3.19) will then become

$$\Omega_0 = \omega_i \frac{2n_{01}v(\hat{\mathbf{q}})}{c} \tag{3.32}$$

$$\Omega_\alpha = \omega_i \frac{2n_{\alpha 1}v(\hat{\mathbf{q}})}{c} \sqrt{1 - \frac{\sin^2 \alpha}{n_{\alpha 1}^2}} \tag{3.33}$$

Which leads to

$$R = \frac{\Omega_\alpha}{\Omega_0} = \frac{n_{\alpha 1}}{n_{01}} \sqrt{1 - \frac{\sin^2 \alpha}{n_{\alpha 1}^2}} \tag{3.34}$$

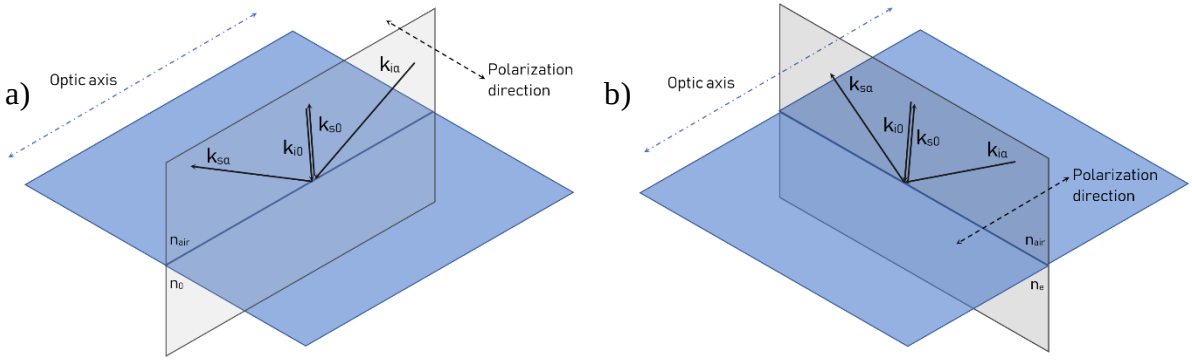

Figure 3.6 Uniaxial material scattering scenarios. (a) Configuration for ordinary index of refraction probing, with optic axis orthogonal to light polarization and parallel to scattering plane. (b) Configuration for extraordinary refractive index measurement with optic axis parallel to light polarization and perpendicular to the scattering plane.

It is straightforward to see that, if the scattering plane is parallel to the optic axis, $\varphi=0$; Since the polarization is orthogonal to the scattering plane, it results $\psi=\pi/2$, which leads to $n(\psi,\varphi)=n_{ord}$ for every incident angle. In this scenario, represented in Fig. (S1a), both scattering geometries will probe n_{ord}, and Eq. (3.20) becomes

$$n_{ord}^2 = \frac{\sin^2 \alpha}{1 - R^2} \tag{3.35}$$

When instead the polarization of the light is parallel to the optic axis, ψ=0 and the probed index of refraction can vary following the optical ellipsoid.

$$\frac{n^2}{n_{ord}^2}\cos^2 \varphi + \frac{n^2}{n_{ext}^2}\sin^2 \varphi = 1 \tag{3.36}$$

The index of refraction is then,

$$n^2 = \left(\frac{\cos^2 \varphi}{n_{ord}^2} + \frac{\sin^2 \varphi}{n_{ext}^2}\right)^{-1} \tag{3.37}$$

A peculiar case of Eq. (3.37) is the one in which the optic axis is perpendicular to the scattering plane as well, since in this condition φ=π/2 for every incident angle (fig S1b). Consequently, Eq. (3.20) becomes

$$n_{ext}^2 = \frac{\sin^2 \alpha}{1 - R^2} \tag{3.38}$$

In the case of a sample with more than one optic axis, a measurement in the described configuration would be possible if the birefringence, i.e. the difference in refractive indexes along different axes, is smaller than the instrument resolution. Otherwise, the proposed method needs to be modified to feature additional geometries and measurement configurations.

3.7 Conclusions

In summary, we have demonstrated that the dual photon-phonon scattering measurement of the frequency shift can provides the real part of the index of refraction n_1 and the speed of sound v, while the measurement of the linewidth in the two geometries provides

the imaginary part of the refractive index n_2 and the sound attenuation coefficient Γ. These quantities can be measured directly and locally with micrometric three-dimensional resolution within a standard confocal microscope in epi-detection configuration

The possibility of retrieving material refractive index using photon-phonon scattering had been proposed three decades ago [104-107]. Our approach brings three crucial innovations to earlier methods. First, at a fundamental level, we devised the co-localization of two scattering geometries to probe the same phonon axis so that anisotropies in the physical properties of the sample do not affect the refractive index measurement. Second, our confocal sampling of the probed volume of interaction provides mapping capabilities at high 3D resolution. Third, our common lens configuration only needs to access samples from one side. From a practical standpoint, we have also developed much faster Brillouin spectrometer that enable mapping of the refractive index.

The uncertainty on the refractive index measurement can be determined from Eq. (3.20). One potential source of uncertainty is the evaluation of the angle α, but the angle can be calibrated with high precision. Here, we fitted α value using three reference materials of known refractive index and Brillouin shift; other methods to determine the angle of incidence of the α-geometry beam can be implemented [108]. The uncertainty on the refractive index can be expressed as linear function of the shift measurement precision. In our experiment, we reached a refractive index precision of ~0.001 using a laser power of 15mW and exposure time of ~s. We operated in shot noise conditions, thus the frequency shift precision improves with the square root of the signal-to-noise ratio.

A potential source of error comes from the asymmetric broadening of the Brillouin linewidth due to the spread of angle illuminated and collected by the objective lens. In our low

NA conditions, such broadening would induce an estimation error of ~0.3% of the shift but was avoided by experimental calibration with materials of known Brillouin shift. At higher NA, this error may increase, however it can be effectively eliminated either by modeling the broadening term for known illuminating-collecting geometry [109], or by adjusting the Lorentzian fit to dismiss asymmetric broadening artifacts [110]. Another potential source of error comes from the acoustic dispersion of the material. The derivation of Eq. (11) assumes constant speed of sound at the frequencies of the two scattering geometries and thus it needs to be modified if acoustic dispersion is significant. However, a linear behavior, i.e. no acoustic dispersion, in the gigahertz frequency range has been reported in many liquid and solid materials [111-118].

CHAPTER 4: THREE DIMENSIONAL COMPLETE OPTICAL AND MECHANICAL CHARACTERIZATION

In this final chapter we will discuss a dual-geometry Brillouin microscopy approach that enables both optical and mechanical characterization of the sampled scattering volume. Conceptually, this technique has similar experimental setup as the one presented in the last chapter. However, we fully took advantage of the dual phonon-photon interaction, achieving the mapping of frequency shift, refractive index, speed of sound, and kinematic viscosity with confocal resolution. Moreover, we implemented a series of improvements to increase spatial resolution, acquisition speed and spectral resolution. Furthermore, through some considerations on the dependance of Brillouin peak intensity on the total polarization, we proposed a density mapping approach, thus also retrieving complex longitudinal modulus. Finally, we also showed how in high optical absorption samples, it could be possible to retrieve the complex refractive index, through the measurement of Brillouin linewidth in two different geometries.

4.1 Material characterization through Brillouin scattering

Since its discovery, Brillouin scattering has been widely used for material characterization of gases, crystal, liquids and more. The scope of possible characterizations goes beyond simply measuring Brillouin shift or refractive index, and generally can be split direct and indirect dependencies. Let's rewrite the expression for Brillouin shift and linewidth combining eq. 3.14 with the expression of longitudinal phonon velocity in eq. 1.4:

$$\Omega = 2\frac{\omega_i}{c} n_1(\omega_i)\sqrt{\frac{M(\hat{\mathbf{q}},\Omega)}{\rho}}\sin\frac{\theta}{2} \tag{4.1}$$

This equation shows a direct relationship between Brillouin shift and refractive index, density and stiffness tensor components. As a result, measuring Brillouin shift along different phonon directions, with the right combination of scattering geometries can lead to direct measurements of stiffness and refractive index [73,119,120]. A similar reasoning can be done with the spectral linewidth, with a direct correlation to kinematic viscosity through equation 3.17:

$$\Delta\Omega = \Gamma(\hat{\mathbf{q}}, \Omega)\mathrm{q}^2 = \frac{M''(\hat{\mathbf{q}}, \Omega)}{\rho}\mathrm{q}^2 \tag{4.2}$$

Where we assumed a non absorbing material, so that $\mathrm{n}_2 = 0$. We can define the complex longitudinal modulus as $\mathrm{M}^* = \mathrm{M}' + \mathrm{iM}''$.

These direct correlations can also be exploited to measure other quantities indirectly. For instance, temperature changes will affect density and refractive index, leading to a modification in the Brillouin signature. In controlled conditions, these second order relationships have been exploited to measure temperature [121], solute concentrations [122], pressure [123], phase state [124], hydration [125], ion concentration [126], and more.

Given the complexity of chemical composition, local water content, and transport phenomena in biological complex, such second order characterization is not viable if not in extremely controlled conditions [127]. We instead focused on direct measurements of complex longitudinal modulus, refractive index, and density.

4.1.1 Extracting refractive index, speed of sound and kinematic viscosity

In this second iteration of our dual-geometry photon-phonon scattering mapping, we choose a slightly different scattering geometry as reported in Figure 4.1. The fundamental difference from the approach taken in Chapter 3 is the relaxation on the condition of same phonon axis measurement, which leads to a direct measurement even in mechanical anisotropy conditions. With this approach the angle between $\hat{\mathbf{q}}_\alpha$ and $\hat{\mathbf{q}}_0$ is about 10 degrees, which means that our measurements remain valid in the conditions of weak anisotropies in mechanical properties. In cases in which anisotropy is not negligible, like in the highly aligned corneal tissue [Josh paper], such measurement can still be performed only if the anisotropic behavior is mathematically or experimentally characterized a priori.

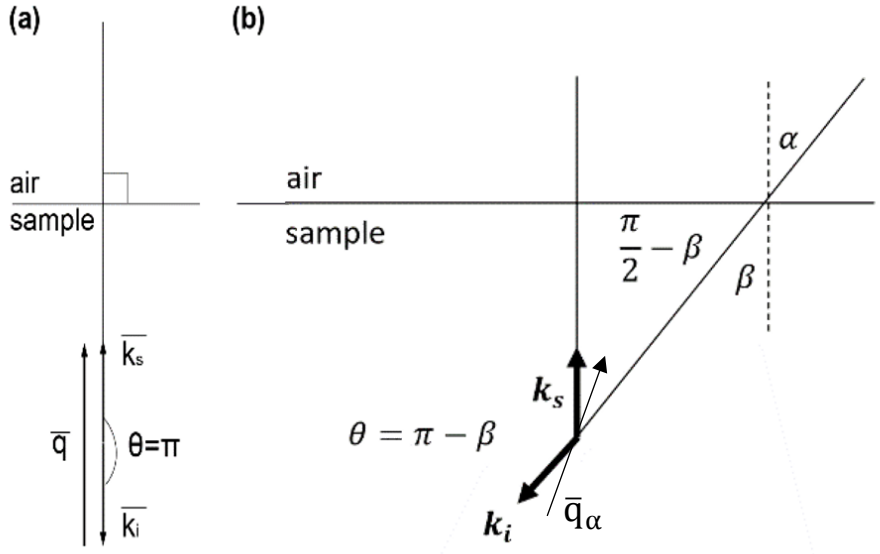

Figure 4.1 Evolved configuration for dual photon-phonon scattering (a) 0-geometry configuration; (b) α-geometry configuration. The difference in the sampled phonon can be observed.

The main advantage of such experimental condition is an improved signal strength in the α-geometry due to scattering probability distribution, which leads to exposure time up to 3 times lower. This is due to a cosine dependency in the photon probability distribution over

different angular positions in the focal plane. As a result, the closer the selected geometry to the optical axis, the higher the probability to collect photons on that path. The optical axis is the central direction orthogonal to the lens where the 0-geometry is built. Thus, a tradeoff is introduced since the lower the distance from the optical axis for the α-geometry, the higher is the spectral overlap between the two shifts, which reduces sensitivity to refractive index and phonon speed. In this case, the Brillouin shift for each geometry will be:

$$\Omega_0 = \frac{2\,\mathrm{nv}}{\lambda} \tag{4.3}$$

$$\Omega_\alpha = \frac{2\,\mathrm{nv}}{\lambda}\cos\frac{\beta}{2} \tag{4.4}$$

Thus, solving the system of two equation we can retrieve an expression for n and v we obtain:

$$\mathrm{n} = \frac{\sin\,\alpha}{\sin(2\arccos\mathrm{R})} \tag{4.5}$$

$$\mathrm{v} = \frac{\lambda\Omega_0}{2}\,\frac{\sin\,(2\arccos\mathrm{R})}{\sin\alpha} \tag{4.6}$$

Similarly, Γ can be extracted with the following expression derived from eq. 4.2:

$$\Gamma = \frac{\mathrm{q}_0^2}{\Delta\Omega_0} = 4\frac{\omega_\mathrm{i}^2}{\mathrm{c}^2}\frac{\mathrm{n}^2}{\Delta\Omega_0} \tag{4.7}$$

Physically, the linewidth is determined by the inverse of the phonon lifetime. In other words, the stronger the sound attenuation within the material, the wider the Brillouin peak. Hence, given that sound attenuation is an energy dissipation, we found that linewidth is a function of viscosity [6]:

$$\Gamma = \frac{M''}{\rho} = \frac{1}{\rho}\left[\frac{4}{3}\eta_S + \eta_b + \frac{\kappa}{C_p}(\gamma - 1)\right] \tag{4.8}$$

Where we M'' is the longitudinal loss modulus, ρ is the density, η_s and η_b are the shear and bulk viscosity, κ is the thermal conductivity, C_p is the isobaric specific hear, and γ is the specific heat ratio. For most materials however the thermodynamic component is negligible since $\gamma \sim 1$, which makes Brillouin linewidth a direct proxy for viscosity. Sometimes, however, it is not possible to decouple the viscosity from the density. In such case it can be useful to define the concept of kinematic viscosity $K = \eta/\rho$. It then becomes immediately clear how the sound attenuation factor Γ is essentially a measurement of kinematic viscosity in the Brillouin frequency range.

4.1.1 Density considerations

From the discussion above it is clear how it is possible to extract the complex refractive index from dual-geometry Brillouin experiment. We also showed it is possible to measure the speed of the phonon as well as its attenuation:

$$v^2 = \frac{M'}{\rho} \qquad\qquad \Gamma = \frac{M''}{\rho} \tag{4.9}$$

It is evident how a complete and direct mechanical characterization would require the knowledge or the measurement of the local density. Traditionally, literature values of the density have been used for the sample that is being measured; but those are usually average values that do not take into account local fluctuations due to changes in biochemical compositions, mechanics or thermodynamics. Hence, in this paragraph we discuss a potential approach to retrieve density still using Brillouin scattering.

From equation 3.8 we know that the Brillouin scattered electric field is proportional to the total polarization in the medium P:

$$\mathbf{E_s} = \chi\epsilon_0 \boldsymbol{P} \sim \rho \frac{\partial \epsilon}{\partial \rho} \tag{4.10}$$

And the intensity of the electric field will be proportional to the number of collected photons:

$$|E_s|^2 \sim |P|^2 \sim N_{photons} \tag{4.11}$$

Given that Brillouin peaks in the frequency space have a Lorentzian shape (eq. 3.16), which has the following general equation:

$$L(\omega) = A \frac{(\Delta\Omega/2)^2}{(\Delta\Omega/2)^2 + (\omega - \Omega)^2} \tag{4.12}$$

The total number of photons collected will be proportional to the integral of Lorentz function over the peak:

$$N_{photons} \sim \int_{peak} L(\omega) d\omega = A\ \Delta\Omega \tag{4.13}$$

Let's now consider the Lorentz-Lorenz relation between index of refraction and polarizability:

$$\frac{n^2 - 1}{n^2 + 2} = \frac{4}{3}\pi N \alpha_m \tag{4.14}$$

Where N is the total number of molecules in the considered volume and α_m is the mean polarizability of the single molecule. The right side of equation 4.14 is an expression of the total polarization of the medium P.

This relationship, which comes from empirical observations of a range of materials [128], is a direct consequence of the Clausius-Mossotti relationships [129-131], that links the

material permittivity to its polarizability. Intuitively, this equation states the direct correlation between the ability of an electric field to polarize molecules in the medium, and the velocity such electric field propagates; Specifically, the higher the polarizability, the higher the refractive index.

Combining eq 4.13 and 4.14, we can then write a Lorentz-Lorenz relationship for the Brillouin scattering volume:

$$\frac{n^2-1}{n^2+2} \propto (A\ \Delta\Omega)^{\frac{1}{2}}\rho \tag{4.15}$$

Which relates the density ρ to the index of refraction n, the intensity of the Brillouin peak A and the Brillouin linewidth $\Delta\Omega$. The expression of the density is:

$$\rho \propto \frac{n^2-1}{n^2+2}(A\Delta\Omega)^{-\frac{1}{2}} \equiv LLB \tag{4.16}$$

Where for the sake of simplicity we defined the right side of the equation as Lorentz-Lorenz-Brillouin factor. Being a proportionality relationship, equation 4.16 does not provide a direct measurement of density through LLB. This is the consequence of two aspects: for once, the dependency expressed in eq. 4.10 refers strictly to isotropic molecules. For highly anisotropic molecules, molecule polarizability and orientation both play a role in determining the polarization induced by the electric field. This is not expected to be an issue in most biological materials because, but nevertheless, it is a possibility. The second point regards the effective number of Brillouin photons. The empirical knowledge of instrumental insertion losses and camera quantum efficiency can lead to relate effectively camera counts to Brillouin photons; nevertheless, fluctuations in local thermodynamic, and fluctuation in refractive index distribution in a complex sample can cause the significant fluctuation in the Brillouin peak

amplitude over time. This artifact can be significatively attenuated by using the alpha geometry to measure the Brillouin peak amplitude, because of its lower sensitivity to back-reflections. As a result, we can still build a calibrated curve between LLB and density thanks to the dependency in equation 4.16, but no direct measurement expression can be written. Despite the limitations, this remains a remarkable measurement, since it decouples density from phonon mechanics, allowing access to longitudinal modulus and viscosity information.

4.3 Experimental Methods

4.3.1 High-resolution dual-geometry Brillouin microscope

The experimental setup described in 3.3.1 lacked the necessary speed and spatial resolution to achieve measurement in biological system. Thus, a series of modification were introduced to achieve micron-scale spatial resolution, and sub-second acquisition time; as mentioned, we modified the scattering geometries to improve signal strength, allowing higher signal and lower exposure time. The improvement of resolution was accomplished through beam shape engineering that guaranteed a high resolution as well as excellent scattering volume overlap. The resulting setup built following these principles is described in Figure 4.2.

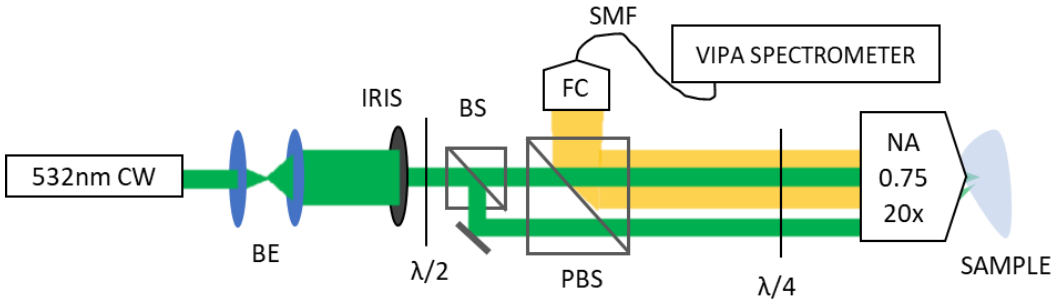

Figure 4.2 Schematic of the experimental setup. BE: beam expander; BS: beam splitter; $\lambda/2$: half wave plate; $\lambda/4$: quarter wave plate; PBS: polarizing beam splitter; FC: fiber coupler; SMF: single mode fiber.

A 532nm continuous wave laser beam is linearly polarized along the P axis via a half-wave plate; subsequently, the beam is expanded to a diameter of approximately 20 mm and then truncated with an iris to a beam of 6 mm diameter. The resulting truncated Gaussian beam guarantees excellent beam separation with a resolution performance similar to flat top beam. This part is thus crucial to enable sub-micron resolution without fundamentally changing the experimental method. This beam is then split into two parallel beams via a beam splitter. The incident beams are transmitted through a polarizing beam splitter thanks to their P polarization, and then converted to a circular polarization through a quarter wave plate. Both beams are focused into the sample through a dry 20x 0.75NA objective lens. The first beam is on the optical axis, i.e. at 0° incidence angle and its corresponding scattered light is also collected on the optical axis. The second incident beam is off-axis at 4 mm from the center of the lens at an angle α=20° and its corresponding scattered light is collected along the center axis. The polarization of the scattered light is mostly preserved, which allows it to be converted to S-polarization on the collection path, and then reflected by the polarizing beam splitter. The scattered light (in yellow) for both geometries is coupled into the same single mode optical fiber acting as confocal pinhole, thus collecting light only from a microscopic 3D region within the sample. To facilitate collection of scattered photons from the proper scattering geometry, the two beams are alternated by a system of two shutters.

Measuring a wide variety of samples with the spectrometer described in 1.2.3 can be challenging because of the limited FSR, that is usually picked and optimized for specific applications, and range; if the Brillouin frequency shift is too close to the condition $\Omega = FSR/2$, the Stokes and anti-Stokes peaks will overlap at the center of the FSR, potentially disrupting the measurement or at least reducing its precision. To avoid this issue, we built a

VIPA that has two etalons with different FSR were used, specifically 17 and 20 GHz. This FSR mismatch generates a multiplexed effect that distributes the light over a plane, instead of the simple diagonal of the two dispersion axis. Visually this FSR 'folding' effect can be represented by figure 4.3, with the extension of the dispersion axis to multiple diagonal lines. As a result the overall effective FSR as follows [132]:

$$FSR_{eff} = \frac{FSR_x * FSR_y}{MCD(FSR_x, FSR_y)} = \frac{(17GHz * 20GHz)}{1\ GHz} = 340GHz \qquad (4.17)$$

These 340 GHz will be distributed over multiple parallel lines. Thus, the effective spectral resolution is substantially unchanged.

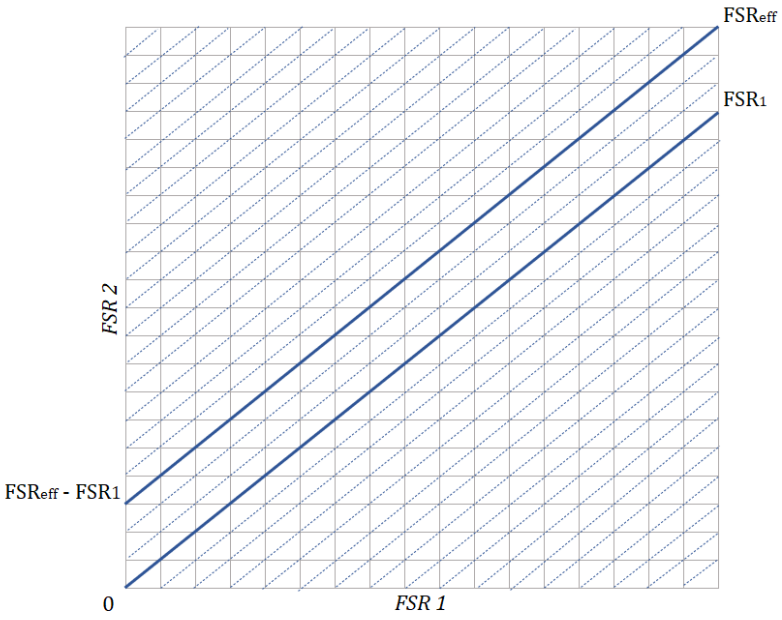

Figure 4.3 Dispersion directions of VIPA spectrometer traced over the plane formed by the two main FSR. The main dispersion direction (0+FSR_1 and FSReff-FSR_1) are highlighted since most material Brillouin signals will lay on these. Secondary dispersions axes are also traced with dotted lines for better representation of the multiplexing effect.

4.3.2 Resolution characterization

In order to characterize the higher resolution of this instrument we imaged the point-spread function of both geometries in three dimensions using a translational stage and a camera. The results in figure 4.4 show the overlap of the two PSF on the XZ and YZ axis. We computed the scattering volume overlap to be 92%. The probed resolution, calculated as the worst dimension between the two PSF along each axis, results to be 0.55 μm by 0.64 μm lateral and 1.43 μm axial.

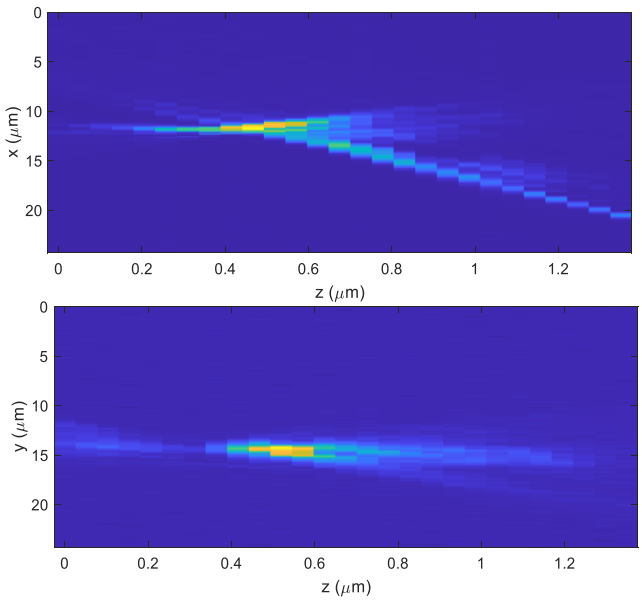

Figure 4.4 Spatial overlap of PSF on XZ plane (top) and YZ plane (bottom). The angle between the two geometries is clear on the XZ plane, while on the YZ plane they appear perfectly parallel.

Next, we characterized the axial confocal resolution of the two geometries to measure the overlap of the confocal plane. In figure 4.5 we reported the Brillouin signal intensity transition of distilled water. The measured distance values are normalized by the refractive index of water, to take into account the difference between optical and geometrical path of the light.

We reported a resolution of ~1.45μm with a confocal plane shift of approximately 0.35μm. This difference can become relevant when measuring at extremely high resolution, but since it has been characterized, it can be corrected in image post processing as a systematic error.

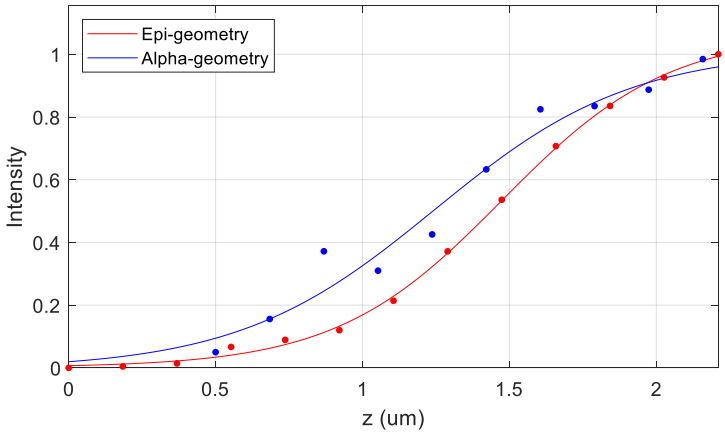

Figure 4.5: Intensity transition of Brillouin water signal for Epidetection 0-geometry and α-geometry.

4.3.3 Linewidth measurement and deconvolution

In order to accurately measure the Brillouin peak linewidth, we implemented a deconvolution algorithm to separate the contribution of phonon lifetime from the spectral PSF. The algorithm's stratefy was first described by Vandewal and Mudare [133] and based on an iterative process. Given $T^{(n)}$ the deconvolved spectrum at the nth-iteration, M the measured spectrum and R the response function of the spectrometer, we define

$$\mathrm{T_i^{(n+1)}} = \mathrm{T_i^{(n)}} \sum_{\mathrm{k}} \frac{\mathrm{R_{ki} M_k}}{\sum_{\mathrm{j}} \mathrm{R_{kj} T_j^{(n)}}} \tag{4.18}$$

Where the indexes refer to pixel number. The starting assumption is usually $T^{(0)} = M$. The deconvolution requires a certain number of iterations to converge, in our case between 5 and 10 depending on the performed experiment and the noise level. Given known values of

Brillouin linewidth, like 500 MHz for water at 532 nm wavelength, we verified the accuracy of the deconvolution process for every experiment as part of instrumental general calibration. The response function is usually measured acquiring the unshifted laser light on the camera, since the instrumental laser linewidth is in the kilohertz range, and it can be considered negligible.

4.4 Results and Discussion

4.4.1 Refractive index measurement

Using the dual geometry approach, we proved our refractive index measuring capabilities in different materials including common laboratory substances (fig. 4.6). For consistency all experiments were performed at 22 degrees Celsius controlled environment, while an Abbe Refractometer was used to measure the RI independently.

Good refractive index accuracy requires instrumental calibration, which was performed using three standard materials: distilled water (n=1.3330), ethanol (n=1.3612) and N2 viscosity standard (n=1.4268). Exposure time is adjusted for every material to reach about 25 thousand counts on camera for optimal precision. As a reference, the exposure time for water is 90ms for 0-geometry and 400ms for α-geometry, with an overall ~10-fold improvement in speed when compared to the similar experiment described in paragraph 3.3.2.

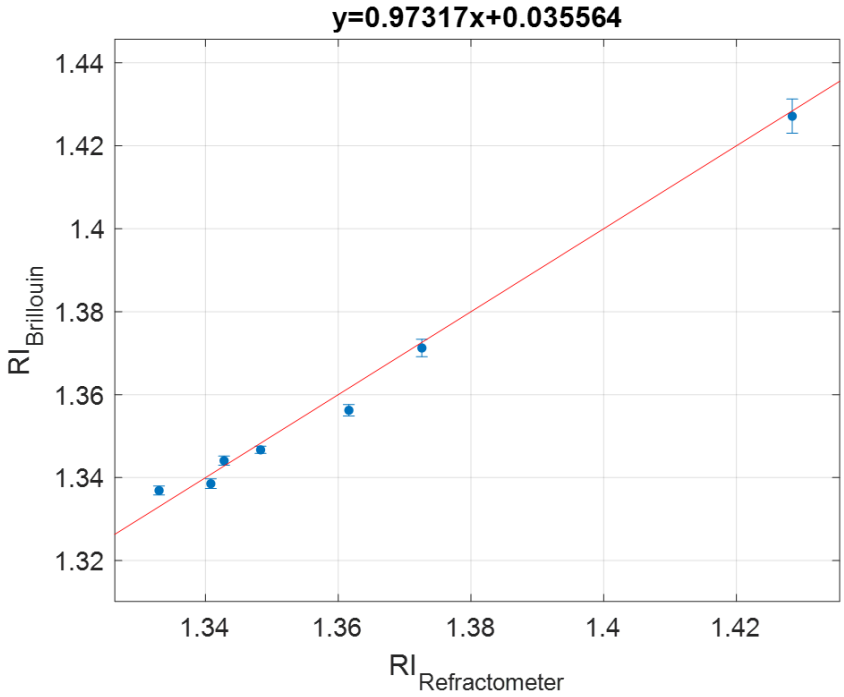

Figure 4.6: Refractive index measurement in different chemicals. The red line shows the theoretical trend of slope 1 and intercept 0 (y = x). The equation on top shows fitted curve equation (R^2=0.992). Error bars represent standard error measured over N=100 measured frames.

4.4.2 Speed of sound measurement

Using the system of equations Eq. 4.7-4.8 we also recovered speed of sound of the same set of materials. We were able to decouple the refractive index from the speed of sound information, as shown in Figure 4.7.

It is clear how the multiple information retrieved allows an easy classification of materials based of their properties. This model could potentially be applied to collection of large data sets in which Brillouin frequency shift alone is not sufficient.

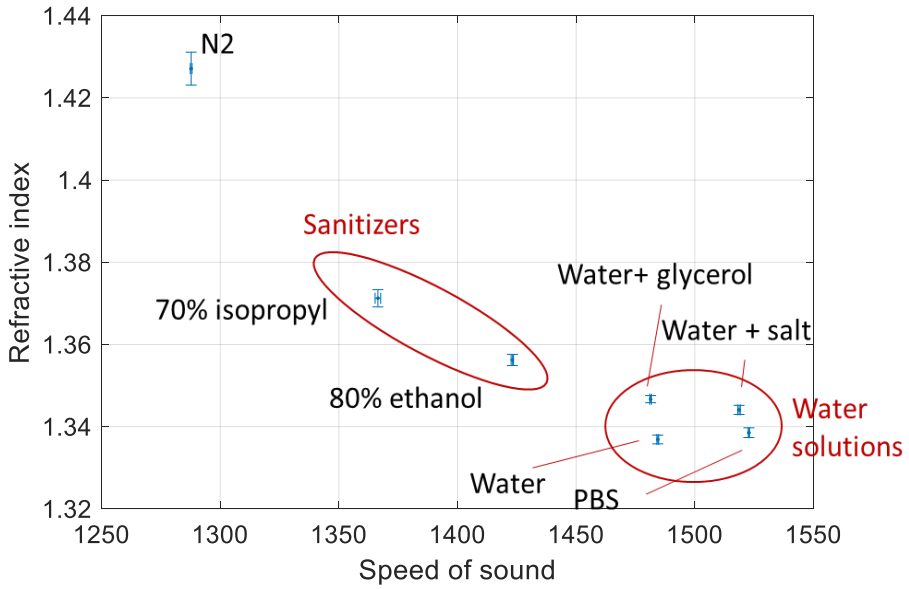

Figure 4.7 Refractive index vs Speed of sound distribution. This data visualization allows rough classification of chemical nature based of the position of the material on the plane. Error bars represent standard error measured over N=100 measured frames.

4.4.3 Kinematic viscosity measurements

To verify our ability to retrieve the kinematic viscosity from the linewidth measurement and deconvolution we measured a set of viscosity standards. The standards were purchased by a manufacturer (Cannon, USA) that provided characterization values that include density, viscosity and kinematic viscosity.

In figure 4.8 the complete characterization of these standards including refractive index, speed of sound and attenuation coefficient. Specifically, we report the measured correlation between the sound attenuation coefficient and. Kinematic viscosity. The correlation we found is on a logarithmic scale which indicates a power law relationship. This kind of correlation might be due to nonlinearity of sound attenuation in the frequency space, because

the kinematic viscosity is typically measured at low frequencies, while Brillouin phonon are in the gigahertz range.

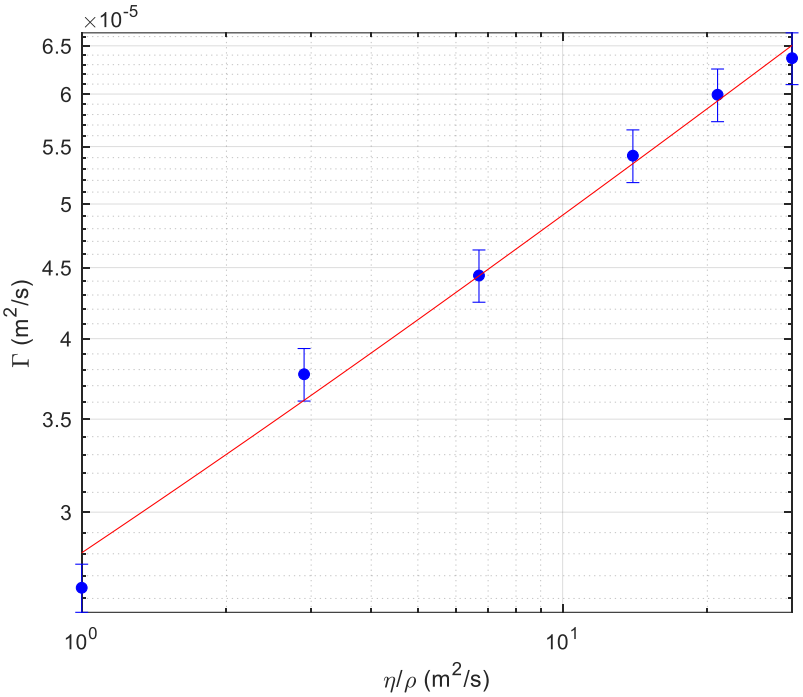

Figure 4.8: Correlation between phonon attenuation and kinematic viscosity. Red line shows power law fit (R^2=0.992). Error bars represent standard error measured over N=100 measured frames.

4.4.4 Density measurements

We report the proof-of-principle that density can be extracted by Brillouin measurements. The measurement was performed in the same set of viscosity standards previously used. For all materials we considered the height of the fitted Lorentzian peak normalized by the exposure time of the specific material. This quantity was used to calculate the LLB coefficient introduced in Eq. 4.16

$$LLB = \frac{n^2 - 1}{n^2 + 2}\left(\frac{A\,\Delta\Omega}{\mathrm{t_e}}\right)^{-\frac{1}{2}} \tag{4.19}$$

Where n is the refractive index, A is the amplitude of the peak, t_e is the exposure time and $\Delta\Omega$ is the Brillouin linewidth. We report in figure 4.9 the correlation between the density of the viscosity standard (as reported by the manufacturer) and the LLB coefficient measured with our setup.

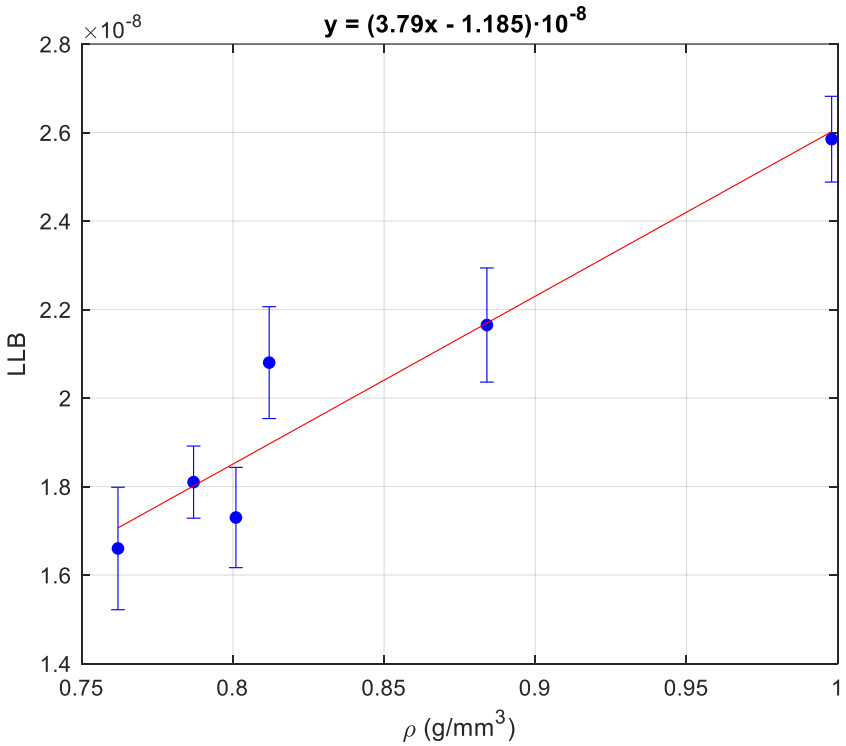

Figure 4.9 Reported correlation between density and LLB coefficient. On top we ported fitted equation. Red line shows fitted curve, R^2=0.913. Error bars represent standard error measured over N=50 measured frames.

Despite this model relying on simple considerations, we found a solid correlation between the two quantities, supporting the hypothesis of LLB coefficient being a proxy for density measurement.

4.4.5 Complete characterization of simple liquid-liquid phase separation

As demonstration of our material characterization capability, we imaged a simple liquid-liquid phase separation system. Liquid-liquid phase separations are state of clear division between two liquids without a physical barrier; for chemical or thermodynamical reasons the components of such system do not mix. A classic example in this sense are water and lipids. Lipid molecules are strongly hydrophobic and, in most cases, do not mix with water molecules. As a result, a separation layer is created. The same can happen in a vast set of biological instances [134], driven by protein [135,136], nucleic acid [137], lipids [138], and other aggregates.

In our experiment, as a proof of principle of our mechanical mapping capabilities in 3D, we used a small mineral oil (ThermoFisher, USA) droplet immersed in distilled water, which recreates a simple LLPS system. The results are reported in figure 4.10, showing complete characterization and correct values for spatial distribution

To obtain the values showed in the figure above we used the correlation relationship obtained with the material characterization. This allowed to retrieve values in the correct units and resulted in accurate numbers for both water and mineral oil. The density mapping seems to have a visible edge artifact, probably due to a fluctuation in light intensity induced by the refractive index interface. As a result of the modulus-density coupling, such artifact is also visible in the complex modulus mapping.

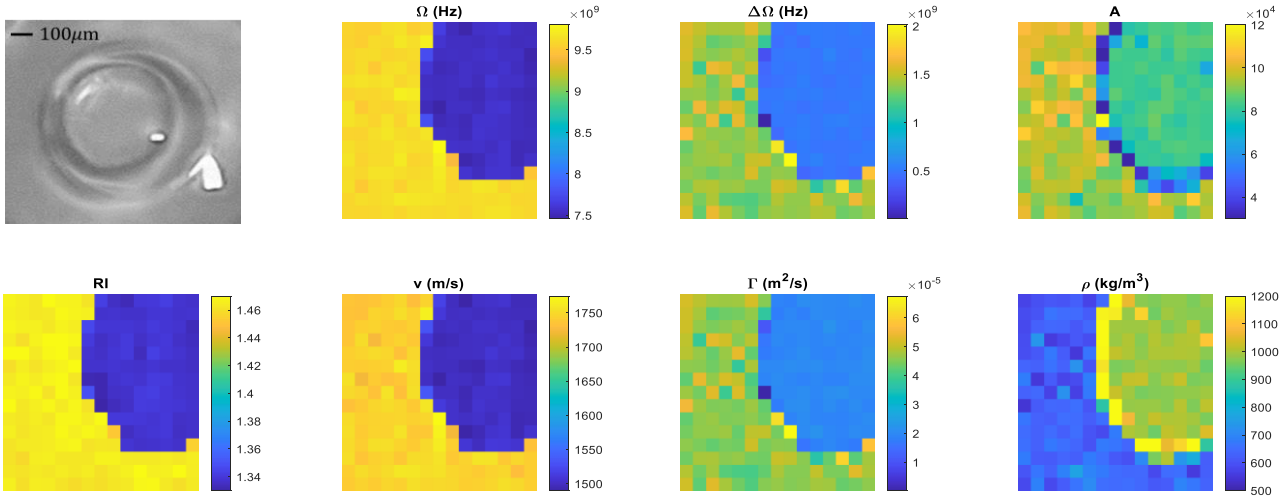

Figure 4.10: Complete characterization of a LLPS system. Top row, right to left: Brightfield image of mineral oil droplet, Brillouin frequency shift distribution, Brillouin linewidth, and Brillouin peak amplitude. Bottom row, from left to right: mapping of refractive index, speed of sound, sound attenuation and density.

This experimental model, despite its simplicity, showcases an artifact that can occur when measuring heterogenous samples. Specifically, Brillouin shift of oil is higher than water, but its density is lower and so is its longitudinal modulus. Our mapping correctly reports these differences, unraveling the opto-acoustic coupling within the Brillouin frequency shift.

4.5 Conclusions

In this chapter we showed how a meticulous analysis of Brillouin spectra can provide a wide variety of sample information. This approach takes full advantage of phonon-photon scattering complexity and breaks down some trivial artifact that can be encountered when performing Brillouin spectroscopy. In particular, we successfully achieved mapping of refractive index, stiffness, density and viscosity with submicron confocal resolution.

Thanks to this novel, unique and multidimensional analysis, we showed the potential of characterizing samples like liquid-liquid phase separation systems in quantitative and label-free manner. Such potential also applies to a broad range of samples that can benefit of such complete characterization such as tumor cells and nodules, corneal tissue, protein aggregates, cellular and nuclear mechanics and more.

CHAPTER 5: CONCLUSIONS AND FUTURE DIRECTIONS

In most cases Brillouin microscopy as performed at the current state of art, remains a strong tool for mechanical characterization since, for water based biological materials, density and refractive index are correlated and proportional to one another. The improvements in Brillouin spectroscopy technique presented in this work can enable this biomechanical imaging in highly scattering and opaque biological materials, with the speed of acquisition typical of VIPA based instruments. Such advancements can lead specific contributions in the near and medium-term future, such as cardiovascular (through atherosclerotic plaques), neurological (through amyloid plaques), ophthalmic (through cataract and lens) and bone structure studies. Here we presented the design, characterization, and principles of a new class of instruments, and these are few potential examples of application and potential studies; however only time can and will provide a more complete set of applications of such technique.

A side note can be made on the single etalon approach for VIPA spectroscopy, that remains an engineering achievement for laboratories or companies with the intent to reduce cost or space taken by a Brillouin spectrometer device. On a biomedical standpoint there is probably not a unique application for such instrument, but on the engineering point of view,

this implementation might make Brillouin microscopy more accessible to a larger number of scientists and researchers.

On the biophysics level, it is important to remark the importance of surpassing the n^2/ρ constant ratio assumption. For instance, in corneal tissue like in most biomaterials, estimation of n^2/ρ ratio variations result to be around 0.3% [139], and its values remains fairly constant in different experimental conditions. These observations suggest that in water based materials n^2/ρ ratio has a minimal effect on Brillouin frequency shift, hence Brillouin becomes a strong proxy for longitudinal modulus. However, dramatic changes in composition within a water based sample, exactly like a liquid-liquid phase separation, breaks this n^2/ρ independence, and can introduce artifacts in Brillouin shift to mechanical mapping correlation. Hence, our approach offers a strong solution to these kinds of scenarios. Biological systems that can present such artifacts include but are not limited to protein aggregates, adipocytes, nucleoli and nucleic acid condensations, and cataract.

Moreover, as discussed in chapter 3, opto-mechanical anisotropy can affect the dual geometry measurement, especially in this last iteration with the sampling of two different phonon axes. Corneal tissue is an ideal example of such condition, because of its optical and mechanical anisotropy. While the optical anisotropy is below our refractive index sensitivity, being $\sim 5 * 10^{-4}$ RIU, the mechanical anisotropy fluctuation on Brillouin shift has been quantified about in 1% at the angles at which our instrument operates [141], and therefore it can and should be taken into account when performing measurements.

Despite a longer time when compared to classical Brillouin microscopy (0.5s vs 0.05s per spectrum), the higher degree of information acquired constitutes a strong incentive in

adopting this approach for several biomechanical characterization scenarios. In addition, potential improvements to setup, such as the use of 660nm laser source, can allow even higher acquisition times in biological media, thanks to the lower absorption coefficient [140].

On a separate note, we also point out the potential of retrieving the imaginary part of the refractive index in sample with high absorption coefficient, with measurement of linewidth difference in the two geometries. Similarly to the case of refractive index and phonon speed, a system of equation can be solved for the linewidth, leading to the following expressions:

$$n_2 = \frac{n_1}{2} \frac{\Delta\Omega_\alpha - \Delta\Omega_0}{\Omega_\alpha - \Omega_0} \tag{4.20}$$

$$\Gamma = \frac{c^2}{4\omega_i^2} \frac{1}{n_1^2} \left(\frac{\Omega_\alpha \Delta\Omega_0 - \Omega_0 \Delta\Omega_\alpha}{\Omega_\alpha - \Omega_0} \right) \tag{4.21}$$

Although in most biological samples optical absorption is typically minimized due to potential photodamage to cells and tissues, specific experimental conditions, such as the presence of an absorbing biomarker, might allow such measurement.

In conclusion, Brillouin microscopy can then expand its scope to highly heterogeneous analysis in even more complex contexts thanks to the described approach, potentially accessing samples like adipocytes, nucleoli, or protein aggregates in which unpredictable density and refractive index fluctuations can lead to ambiguity and uncertainty. These advancements also require a constant improvement of Brillouin spectrometers in terms of resolution, contrast and throughput. In this direction, we offered few solutions that can be adopted and implemented in future iterations.

References

1. Brillouin, L. (1922). Diffusion de la lumière et des rayons X par un corps transparent homogène. In Annales de physique (Vol. 9, No. 17, pp. 88-122).
2. Brillouin, L. (1920). The theory of solids and quanta. In Scientific Annals of the École Normale Supérieure (Vol. 37, pp. 357-459).
3. Mandelstam, L. I. (1926). Light scattering by inhomogeneous media. Zh. Russ. Fiz-Khim. Ova, 58(381), 146.
4. Chiao, R. Y., Townes, C. H., & Stoicheff, B. P. (1964). Stimulated Brillouin scattering and coherent generation of intense hypersonic waves. Physical Review Letters, 12(21), 592.
5. Bloch, F. (1930). Zur theorie des ferromagnetismus. Zeitschrift für Physik 61.3-4: 206-219.
6. Boyd, R. W. (2020). Nonlinear optics. Academic press.
7. Singh, R. (2002). CV Raman and the Discovery of the Raman Effect. Physics in Perspective, 4(4), 399-420.
8. Landau, L. D., Lifshitz, E. M., & Pitaevskii, L. P. (1992). Electrodynamics of continuous media, 1984. Moscow Science.
9. Einstein, A. (1910). Theorie der Opaleszenz von homogenen Flüssigkeiten und Flüssigkeitsgemischen in der Nähe des kritischen Zustandes. Annalen der Physik, 338(16), 1275-1298.
10. Hayes, W., & Loudon, R. A. (1978). Light Scattering by Crystals.
11. Benedek, G. B., & Fritsch, K. (1966). Brillouin scattering in cubic crystals. Physical Review, 149(2), 647.
12. Landau, L., & Placzek, G. (1934). Structure of the undisplaced scattering line. Phys. Z. Sowiet. Un, 5, 172.
13. Fabelinskii, I. L. (1968). Stimulated molecular scattering of light. In Molecular Scattering of Light (pp. 483-532). Springer, Boston, MA.
14. Millot, G., & Tchofo-Dinda, P. (2005). Basic principles of nonlinear effects in optical fibres. Encyclopedia of Modern Optics.
15. Gross, E. (1930). Change of wave-length of light due to elastic heat waves at scattering in liquids. Nature, 126(3171), 201-202.
16. Gross, E. (1930). The splitting of spectral lines at scattering of light by liquids. Nature, 126(3176), 400-400.
17. Randall, J. T., & Vaughan, J. M. (1979). Brillouin scattering in systems of biological significance. Philosophical Transactions of the Royal Society of London. Series A, Mathematical and Physical Sciences, 293(1402), 341-348..
18. Cusack, S., & Miller, A. (1979). Determination of the elastic constants of collagen by Brillouin light scattering. Journal of molecular biology, 135(1), 39-51.
19. Harley, R., James, D., Miller, A., & White, J. W. (1977). Phonons and the elastic moduli of collagen and muscle. Nature, 267(5608), 285-287.
20. Berovic, N., Thomas, N., Thornhill, R. A., & Vaughan, J. M. (1989). Observation of Brillouin scattering from single muscle fibres. European Biophysics Journal, 17(2), 69-74.
21. Scarcelli, G., & Yun, S. H. (2008). Confocal Brillouin microscopy for three-dimensional mechanical imaging. Nature photonics, 2(1), 39-43.

22. Scarcelli, G., & Yun, S. H. (2007, May). Three-dimensional Brillouin confocal microscopy. In Conference on Lasers and Electro-Optics (p. CTuV5). Optical Society of America.
23. Antonacci, G., Pedrigi, R. M., Kondiboyina, A., Mehta, V. V., De Silva, R., Paterson, C., ... & Török, P. (2015). Quantification of plaque stiffness by Brillouin microscopy in experimental thin cap fibroatheroma. Journal of the Royal Society Interface, 12(112), 20150843.
24. Mattana, S., Caponi, S., Tamagnini, F., Fioretto, D., & Palombo, F. (2017). Viscoelasticity of amyloid plaques in transgenic mouse brain studied by Brillouin microspectroscopy and correlative Raman analysis. Journal of innovative optical health sciences, 10(06), 1742001.
25. Shao, P., Besner, S., Zhang, J., Scarcelli, G., & Yun, S. H. (2016). Etalon filters for Brillouin microscopy of highly scattering tissues. Optics express, 24(19), 22232-22238.
26. Michelson, A. A. (1898). The echelon spectroscope. The Astrophysical Journal, 8, 37.
27. Jacquinot, P. (1954). The luminosity of spectrometers with prisms, gratings, or Fabry-Perot etalons. JOSA, 44(10), 761-765.
28. Perot, A., & Fabry, C. (1899). On the application of interference phenomena to the solution of various problems of spectroscopy and metrology. The Astrophysical Journal, 9, 87.
29. Jacquinot, P. (1954). The luminosity of spectrometers with prisms, gratings, or Fabry-Perot etalons. JOSA, 44(10), 761-765.
30. Hirschberg J. G., (1955). Bulletin American Physical Society 30, No.3, 23.
31. Biondi, M. A. (1956). High-Speed, Direct Recording Fabry-Perot Interferometer. Review of Scientific Instruments, 27(1), 36-39.
32. Chiao, R. Y., & Stoicheff, B. P. (1964). Brillouin scattering in liquids excited by the He–Ne maser. JOSA, 54(10), 1286-1287.
33. Akilbekova, D., Ogay, V., Yakupov, T., Sarsenova, M., Umbayev, B., Nurakhmetov, A., ... & Utegulov, Z. N. (2018). Brillouin spectroscopy and radiography for assessment of viscoelastic and regenerative properties of mammalian bones. Journal of biomedical optics, 23(9), 097004.
34. Sandercock, J. R. (1970). Brillouin scattering study of SbSI using a double-passed, stabilised scanning interferometer. Optics communications, 2(2), 73-76.
35. Lindsay, S. M., Anderson, M. W., & Sandercock, J. R. (1981). Construction and alignment of a high performance multipass vernier tandem Fabry–Perot interferometer. Review of scientific instruments, 52(10), 1478-1486.
36. Scarponi, F., Mattana, S., Corezzi, S., Caponi, S., Comez, L., Sassi, P., ... & Fioretto, D. (2017). High-performance versatile setup for simultaneous Brillouin-Raman microspectroscopy. Physical Review X, 7(3), 031015.
37. Lee, J. Y., Kim, J. W., Yoo, Y. S., Hahn, J. W., & Lee, H. W. (2002). Spatial-domain cavity ringdown from a high-finesse plane Fabry–Perot cavity. Journal of applied physics, 91(2), 582-594.
38. Koski, K. J., & Yarger, J. L. (2005). Brillouin imaging. Applied Physics Letters, 87(6), 061903.
39. Itoh, S. I. (1998). Very rapid nonscanning Brillouin spectroscopy using fixed etalons and multichannel detectors. Japanese journal of applied physics, 37(5S), 3134.
40. Scarcelli, G., & Yun, S. H. (2011). Multistage VIPA etalons for high-extinction parallel Brillouin spectroscopy. Optics express, 19(11), 10913-10922.
41. Scarcelli, G., Kim, P., & Yun, S. H. (2008). Cross-axis cascading of spectral dispersion. Optics letters, 33(24), 2979-2981.

42. Berghaus, K. V., Yun, S. H., & Scarcelli, G. (2015). High speed sub-GHz spectrometer for Brillouin scattering analysis. JoVE (Journal of Visualized Experiments), (106), e53468.
43. Scarcelli, G., Polacheck, W. J., Nia, H. T., Patel, K., Grodzinsky, A. J., Kamm, R. D., & Yun, S. H. (2015). Noncontact three-dimensional mapping of intracellular hydromechanical properties by Brillouin microscopy. Nature methods, 12(12), 1132-1134.
44. Nikolić, M., Conrad, C., Zhang, J., & Scarcelli, G. (2018). Noninvasive imaging: Brillouin confocal microscopy. Biomechanics in Oncology, 351-364.
45. Antonacci, G., Beck, T., Bilenca, A., Czarske, J., Elsayad, K., Guck, J., ... & Scarcelli, G. (2020). Recent progress and current opinions in Brillouin microscopy for life science applications. Biophysical Reviews, 12, 615-624.
46. Prevedel, R., Diz-Muñoz, A., Ruocco, G., & Antonacci, G. (2019). Brillouin microscopy: an emerging tool for mechanobiology. Nature methods, 16(10), 969-977.
47. Bottani, C. E., & Fioretto, D. (2018). Brillouin scattering of phonons in complex materials. Advances in Physics: X, 3(1), 1467281.
48. Conrad, C., Gray, K. M., Stroka, K. M., Rizvi, I., & Scarcelli, G. (2019). Mechanical characterization of 3D ovarian cancer nodules using brillouin confocal microscopy. Cellular and molecular bioengineering, 12(3), 215-226.
49. Scarcelli, G., Kling, S., Quijano, E., Pineda, R., Marcos, S., & Yun, S. H. (2013). Brillouin microscopy of collagen crosslinking: noncontact depth-dependent analysis of corneal elastic modulus. Investigative ophthalmology & visual science, 54(2), 1418-1425.
50. Zhang, J., Alisafaei, F., Nikolić, M., Nou, X. A., Kim, H., Shenoy, V. B., & Scarcelli, G. (2020). Nuclear mechanics within intact cells is regulated by cytoskeletal network and internal nanostructures. Small, 16(18), 1907688.
51. Chan, C. J., Bevilacqua, C., & Prevedel, R. (2021). Mechanical mapping of mammalian follicle development using Brillouin microscopy. bioRxiv.
52. Fiore, A., Zhang, J., Shao, P., Yun, S. H., & Scarcelli, G. (2016). High-extinction virtually imaged phased array-based Brillouin spectroscopy of turbid biological media. Applied physics letters, 108(20), 203701.
53. Sandercock, J. R. (1975). Some recent developments in Brillouin scattering. Rca Rev, 36(1), 89-107.
54. Čopič, M., & Zgonik, M. (1982). On multi-pass Fabry-Perot interferometer. Optics Communications, 41(5), 310-314.
55. Cheong, W. F., Prahl, S. A., & Welch, A. J. (1990). A review of the optical properties of biological tissues. IEEE journal of quantum electronics, 26(12), 2166-2185.
56. Antonacci, G., de Turris, V., Rosa, A., & Ruocco, G. (2018). Background-deflection Brillouin microscopy reveals altered biomechanics of intracellular stress granules by ALS protein FUS. Communications biology, 1(1), 1-8.
57. Shao, P., Besner, S., Zhang, J., Scarcelli, G., & Yun, S. H. (2016). Etalon filters for Brillouin microscopy of highly scattering tissues. Optics express, 24(19), 22232-22238.
58. Antonacci, G., Lepert, G., Paterson, C., & Török, P. (2015). Elastic suppression in Brillouin imaging by destructive interference. Applied Physics Letters, 107(6), 061102.
59. Edrei, E., Gather, M. C., & Scarcelli, G. (2017). Integration of spectral coronagraphy within VIPA-based spectrometers for high extinction Brillouin imaging. Optics express, 25(6), 6895-6903.

60. Meng, Z., Traverso, A. J., & Yakovlev, V. V. (2014). Background clean-up in Brillouin microspectroscopy of scattering medium. Optics express, 22(5), 5410-5415.
61. Schoen, P. E., & Jackson, D. A. (1972). The iodine filter in Raman and Brillouin spectroscopy. Journal of Physics E: Scientific Instruments, 5(6), 519.
62. Lepert, G., Gouveia, R. M., Connon, C. J., & Paterson, C. (2016). Assessing corneal biomechanics with Brillouin spectro-microscopy. Faraday discussions, 187, 415-428.
63. Meng, Z., Bustamante Lopez, S. C., Meissner, K. E., & Yakovlev, V. V. (2016). Subcellular measurements of mechanical and chemical properties using dual Raman-Brillouin microspectroscopy. Journal of Biophotonics, 9(3), 201-207.
64. Meng, Z., & Yakovlev, V. V. (2015). Optimizing signal collection efficiency of the VIPA-based Brillouin spectrometer. Journal of Innovative Optical Health Sciences, 8(04), 1550021.
65. Meng, Z., & Yakovlev, V. V. (2016). Precise determination of Brillouin scattering spectrum using a virtually imaged phase array (VIPA) spectrometer and charge-coupled device (CCD) camera. Applied spectroscopy, 70(8), 1356-1363.
66. Antonacci, G., De Panfilis, S., Di Domenico, G., DelRe, E., & Ruocco, G. (2016). Breaking the contrast limit in single-pass fabry-pérot spectrometers. Physical Review Applied, 6(5), 054020.
67. Traverso, A. J., Thompson, J. V., Steelman, Z. A., Meng, Z., Scully, M. O., & Yakovlev, V. V. (2015). Dual Raman-Brillouin microscope for chemical and mechanical characterization and imaging. Analytical chemistry, 87(15), 7519-7523.
68. Antonacci, G. (2017). Dark-field Brillouin microscopy. Optics letters, 42(7), 1432-1435.
69. Fiore, A., & Scarcelli, G. (2019). Single etalon design for two-stage cross-axis VIPA spectroscopy. Biomedical optics express, 10(3), 1475-1481.
70. Hariharan, P., & Sen, D. (1961). Double-passed fabry-perot interferometer. JOSA, 51(4), 398-399.
71. Fiore, A., & Scarcelli, G. (2021). Multipass etalon cascade for high-resolution parallel spectroscopy. Optics Letters, 46(4), 781-784.
72. Fiore, A., & Scarcelli, G. (2019). Single etalon design for two-stage cross-axis VIPA spectroscopy. Biomedical optics express, 10(3), 1475-1481.
73. Fiore, A., Bevilacqua, C., & Scarcelli, G. (2019). Direct three-dimensional measurement of refractive index via dual photon-phonon scattering. Physical review letters, 122(10), 103901.
74. Fang-Yen, C. M., Choi, W., Sung, Y., Holbrow, C. J., Dasari, R. R., & Feld, M. S. (2011). Video-rate tomographic phase microscopy. Journal of biomedical optics, 16(1), 011005.
75. Koohyar, F. (2013). Refractive index and its applications. J. Thermodyn. Catal, 4(02).
76. Khmaladze, A., Kim, M., & Lo, C. M. (2008). Phase imaging of cells by simultaneous dual-wavelength reflection digital holography. Optics express, 16(15), 10900-10911.
77. Kemper, B., Bauwens, A., Bettenworth, D., Götte, M., Greve, B., Kastl, L., ... & Vollmer, A. (2019). Label-free quantitative in vitro live cell imaging with digital holographic microscopy. In Label-Free Monitoring of Cells in vitro (pp. 219-272). Springer, Cham.
78. Meng, Z., Yao, X. S., Yao, H., Liang, Y., Liu, T., Li, Y., ... & Lan, S. (2009). Measurement of the refractive index of human teeth by optical coherence tomography. Journal of biomedical optics, 14(3), 034010.
79. Tearney, G. J., Brezinski, M. E., Southern, J. F., Bouma, B. E., Hee, M. R., & Fujimoto, J. G. (1995). Determination of the refractive index of highly scattering human tissue by optical coherence tomography. Optics letters, 20(21), 2258-2260.

80. Ilev, I. K., Waynant, R. W., Byrnes, K. R., & Anders, J. J. (2002). Dual-confocal fiber-optic method for absolute measurement of refractive index and thickness of optically transparent media. Optics letters, 27(19), 1693-1695.
81. Meng, Z., Zhai, X., Wei, J., Wang, Z., & Wu, H. (2018). Absolute measurement of the refractive index of water by a mode-locked laser at 518 nm. Sensors, 18(4), 1143.
82. Wei, T., Han, Y., Li, Y., Tsai, H. L., & Xiao, H. (2008). Temperature-insensitive miniaturized fiber inline Fabry-Perot interferometer for highly sensitive refractive index measurement. Optics Express, 16(8), 5764-5769.
83. Trainoff, S. P., & Cannell, D. S. (2002). Physical optics treatment of the shadowgraph. Physics of Fluids, 14(4), 1340-1363.
84. Park, Y., Diez-Silva, M., Popescu, G., Lykotrafitis, G., Choi, W., Feld, M. S., & Suresh, S. (2008). Refractive index maps and membrane dynamics of human red blood cells parasitized by Plasmodium falciparum. Proceedings of the National Academy of Sciences, 105(37), 13730-13735.
85. Schürmann, M., Scholze, J., Müller, P., Guck, J., & Chan, C. J. (2016). Cell nuclei have lower refractive index and mass density than cytoplasm. Journal of biophotonics, 9(10), 1068-1076.
86. Liu, P. Y., Chin, L. K., Ser, W., Chen, H. F., Hsieh, C. M., Lee, C. H., ... & Leprince-Wang, Y. (2016). Cell refractive index for cell biology and disease diagnosis: past, present and future. Lab on a Chip, 16(4), 634-644.
87. Davies, H. G., Wilkins, M. H. F., Chayen, J., & La Cour, L. F. (1954). The use of the interference microscope to determine dry mass in living cells and as a quantitative cytochemical method. Journal of Cell Science, 3(31), 271-304.
88. Wang, Z., Popescu, G., Tangella, K. V., & Balla, A. (2011). Tissue refractive index as marker of disease. Journal of biomedical optics, 16(11), 116017.
89. Wang, P., Bista, R., Bhargava, R., Brand, R. E., & Liu, Y. (2010). Spatial-domain low-coherence quantitative phase microscopy for cancer diagnosis. Optics letters, 35(17), 2840-2842.
90. Patel, S., Marshall, J., & Fitzke, F. W. (1995). Refractive index of the human corneal epithelium and stroma.
91. Meek, K. M., Dennis, S., & Khan, S. (2003). Changes in the refractive index of the stroma and its extrafibrillar matrix when the cornea swells. Biophysical journal, 85(4), 2205-2212.
92. Campbell, M. C. (1984). Measurement of refractive index in an intact crystalline lens. Vision Research, 24(5), 409-415.
93. Merola, F., Memmolo, P., Miccio, L., Savoia, R., Mugnano, M., Fontana, A., ... & Ferraro, P. (2017). Tomographic flow cytometry by digital holography. Light: Science & Applications, 6(4), e16241-e16241.
94. Groso, A., Abela, R., & Stampanoni, M. (2006). Implementation of a fast method for high resolution phase contrast tomography. Optics express, 14(18), 8103-8110.
95. Sung, Y., Lue, N., Hamza, B., Martel, J., Irimia, D., Dasari, R. R., ... & So, P. (2014). Three-dimensional holographic refractive-index measurement of continuously flowing cells in a microfluidic channel. Physical review applied, 1(1), 014002.
96. Fukuda, T., Wang, Y., Xia, P., Awatsuji, Y., Kakue, T., Nishio, K., & Matoba, O. (2017). Three-dimensional imaging of distribution of refractive index by parallel phase-shifting digital holography using Abel inversion. Optics express, 25(15), 18066-18071.

97. Shaked, N. T., Roichman, Y., & Habaza, M. (2017, April). Live Cell Trapping and Rotation for Label-Free Tomography and 3-D Refractive-Index Imaging. In Optical Trapping Applications (pp. OtM4E-3). Optical Society of America.
98. Fabelinskii, I. L. (2012). Molecular scattering of light. Springer Science & Business Media.
99. Kim, M., Besner, S., Ramier, A., Kwok, S. J., An, J., Scarcelli, G., & Yun, S. H. (2016). Shear Brillouin light scattering microscope. Optics express, 24(1), 319-328.
100. Zhang, J., Fiore, A., Yun, S. H., Kim, H., & Scarcelli, G. (2016). Line-scanning Brillouin microscopy for rapid non-invasive mechanical imaging. Scientific reports, 6(1), 1-8.
101. Wang, T. D., Mandella, M. J., Contag, C. H., & Kino, G. S. (2003). Dual-axis confocal microscope for high-resolution in vivo imaging. Optics letters, 28(6), 414-416.
102. Sandercock, J. R. (1972). Brillouin-scattering measurements on silicon and germanium. Physical Review Letters, 28(4), 237.
103. Pajdzik, L. A., & Glazer, A. M. (2006). Three-dimensional birefringence imaging with a microscope tilting stage. II. Biaxial crystals. Journal of applied crystallography, 39(6), 856-870.
104. Zha, C. S., Hemley, R. J., Mao, H. K., Duffy, T. S., & Meade, C. (1994). Acoustic velocities and refractive index of SiO 2 glass to 57.5 GPa by Brillouin scattering. Physical Review B, 50(18), 13105.
105. Jeong, M. S., Kim, J. H., Ko, J. H., Ko, Y. H., & Kim, K. J. (2013). Pressure dependence of acoustic behaviors and refractive index of amorphous Kel F-800 copolymer studied by Brillouin spectroscopy. Current Applied Physics, 13(8), 1774-1777.
106. Parsons, L. C., & Andrews, G. T. (2012). Probing near-normally propagating bulk acoustic waves using pseudo-reflection geometry Brillouin spectroscopy. AIP Advances, 2(3), 032157.
107. Krüger, J. K., Marx, A., Peetz, L., Roberts, R., & Unruh, H. G. (1986). Simultaneous determination of elastic and optical properties of polymers by high performance Brillouin spectroscopy using different scattering geometries. Colloid and Polymer Science, 264(5), 403-414.
108. Penciu, R. S., Kriegs, H., Petekidis, G., Fytas, G., & Economou, E. N. (2003). Phonons in colloidal systems. The Journal of chemical physics, 118(11), 5224-5240.
109. Antonacci, G., Foreman, M. R., Paterson, C., & Török, P. (2013). Spectral broadening in Brillouin imaging. Applied Physics Letters, 103(22), 221105.
110. Corezzi, S., Comez, L., & Zanatta, M. (2018). A simple analysis of Brillouin spectra from opaque liquids and its application to aqueous suspensions of poly-N-isopropylacrylamide microgel particles. Journal of Molecular Liquids, 266, 460-466.
111. Tiganov, E. V. (1966). Dispersion and Absorption of Sound in Water and in Acetone. Soviet Journal of Experimental and Theoretical Physics Letters, 4, 261.
112. Ostwald, J., Pazold, W., & Weis, O. (1977). High-resolution Brillouin spectroscopy of water. Applied physics, 13(4), 351-356.
113. Cusack, S., & Lees, S. (1984). Variation of longitudinal acoustic velocity at gigahertz frequencies with water content in rat-tail tendon fibers. Biopolymers: Original Research on Biomolecules, 23(2), 337-351.
114. O'Connor, C. L., & Schlupf, J. P. (1967). Brillouin scattering in water: the Landau—Placzek ratio. The Journal of Chemical Physics, 47(1), 31-38.

115. Oshima, C., Aizawa, T., Souda, R., Ishizawa, Y., & Sumiyoshi, Y. (1988). Surface phonon dispersion curves of graphite (0001) over the entire energy region. Solid State Communications, 65(12), 1601-1604.
116. Cheng, W., Gomopoulos, N., Fytas, G., Gorishnyy, T., Walish, J., Thomas, E. L., ... & Baer, E. (2008). Phonon dispersion and nanomechanical properties of periodic 1D multilayer polymer films. Nano letters, 8(5), 1423-1428.
117. Krüger, J. K., Embs, J., Brierley, J., & Jiménez, R. (1998). A new Brillouin scattering technique for the investigation of acoustic and opto-acoustic properties: Application to polymers. Journal of Physics D: Applied Physics, 31(15), 1913.
118. Gomopoulos, N., Cheng, W., Efremov, M., Nealey, P. F., & Fytas, G. (2009). Out-of-plane longitudinal elastic modulus of supported polymer thin films. Macromolecules, 42(18), 7164-7167.
119. Koski, K. J., Akhenblit, P., McKiernan, K., & Yarger, J. L. (2013). Non-invasive determination of the complete elastic moduli of spider silks. Nature materials, 12(3), 262-267.
120. Remer, I., Shaashoua, R., Shemesh, N., Ben-Zvi, A., & Bilenca, A. (2020). High-sensitivity and high-specificity biomechanical imaging by stimulated Brillouin scattering microscopy. Nature Methods, 17(9), 913-916.
121. Bao, X., Dhliwayo, J., Heron, N., Webb, D. J., & Jackson, D. A. (1995). Experimental and theoretical studies on a distributed temperature sensor based on Brillouin scattering. Journal of lightwave technology, 13(7), 1340-1348.
122. Adichtchev, S. V., Karpegina, Y. A., Okotrub, K. A., Surovtseva, M. A., Zykova, V. A., & Surovtsev, N. V. (2019). Brillouin spectroscopy of biorelevant fluids in relation to viscosity and solute concentration. Physical Review E, 99(6), 062410.
123. Méndez, A., & Diatzikis, E. (2006, October). Fiber optic distributed pressure sensor based on Brillouin scattering. In Optical Fiber Sensors (p. ThE46). Optical Society of America.
124. Hirschberg, J. G., Wouters, A. W., & Byrne, J. D. (1980). Ocean parameters using the Brillouin effect. Ocean Remote Sensing Using Lasers, 29.
125. Wu, P. J., Kabakova, I. V., Ruberti, J. W., Sherwood, J. M., Dunlop, I. E., Paterson, C., ... & Overby, D. R. (2018). Water content, not stiffness, dominates Brillouin spectroscopy measurements in hydrated materials. Nature methods, 15(8), 561-562.
126. Williams, E. A., Cohen, B. I., Divol, L., Dorr, M. R., Hittinger, J. A., Hinkel, D. E., ... & Glenzer, S. H. (2004). Effects of ion trapping on crossed-laser-beam stimulated Brillouin scattering. Physics of Plasmas, 11(1), 231-244.
127. Scarcelli, G., Yun, S.H. Reply to 'Water content, not stiffness, dominates Brillouin spectroscopy measurements in hydrated materials'. Nat Methods 15, 562–563 (2018).
128. Lorentz, H. A. (1881). "Ueber die Anwendung des Satzes vom Virial in der kinetischen Theorie der Gase". Annalen der Physik
129. Clausius, R. (1879). Die Mechanische Behandlung der Electricität. Wiesbaden: Vieweg+Teubner Verlag
130. Mossotti, O. F. (1846). Discussione analitica sull'influenza che l'azione di un mezzo dielettrico ha sulla distribuzione dell'elettricità alla superficie di più corpi elettrici disseminati in esso (Vol. 22). Dai tipi della r. D. camera.
131. Lorenz, L. (1869). Experimentale og theoretiske Undersøgelser: over Legmernes Brydningsforhold. Bianco Luno.

132. Berghaus, K., Zhang, J., Yun, S. H., & Scarcelli, G. (2015). High-finesse sub-GHz-resolution spectrometer employing VIPA etalons of different dispersion. Optics letters, 40(19), 4436-4439.
133. Vanderwal, J., Mudare, S. M., & Walton, D. (1981). Deconvolution of Brillouin spectra. Optics Communications, 37(1), 33-36.
134. Hyman, A. A., Weber, C. A., & Jülicher, F. (2014). Liquid-liquid phase separation in biology. Annual review of cell and developmental biology, 30, 39-58.
135. Wegmann, S., Eftekharzadeh, B., Tepper, K., Zoltowska, K. M., Bennett, R. E., Dujardin, S., ... & Hyman, B. T. (2018). Tau protein liquid–liquid phase separation can initiate tau aggregation. The EMBO journal, 37(7), e98049.
136. Ambadipudi, S., Biernat, J., Riedel, D., Mandelkow, E., & Zweckstetter, M. (2017). Liquid–liquid phase separation of the microtubule-binding repeats of the Alzheimer-related protein Tau. Nature communications, 8(1), 1-13.
137. Weber, S. C. (2019). Evidence for and against liquid-liquid phase separation in the nucleus. Non-coding RNA, 5(4), 50.
138. Zoni, V., Khaddaj, R., Campomanes, P., Thiam, R., Schneiter, R., & Vanni, S. (2020). Lipid droplet biogenesis is driven by liquid-liquid phase separation. Available at SSRN 3526890.
139. Scarcelli, G., Pineda, R., & Yun, S. H. (2012). Brillouin optical microscopy for corneal biomechanics. Investigative ophthalmology & visual science, 53(1), 185-190.
140. Nikolić, M., & Scarcelli, G. (2019). Long-term Brillouin imaging of live cells with reduced absorption-mediated damage at 660nm wavelength. Biomedical optics express, 10(4), 1567-1580.
141. Webb, J. N., & Scarcelli, G. (2019). Brillouin microscopy measurement of the anisotropic properties of the cornea. Investigative Ophthalmology & Visual Science, 60(9), 6816-6816.